Carbon-Binder Weight Loading Optimization for Improved Lithium-Ion Battery Rate Capability

Francois L. E. Usseglio-Viretta,[1,z] Andrew M. Colclasure,[1] Alison R. Dunlop,[2] Stephen E. Trask,[2] Andrew N. Jansen,[2,*] Daniel P. Abraham,[2,*] Marco-Tulio F. Rodrigues,[2,*] Eric J. Dufek,[3,*] Tanvir R. Tanim,[3] Parameswara R. Chinnam,[3] Yeyoung Ha,[4,*] and Kandler Smith[1]

[1]Center for Energy Conversion & Storage Systems, National Renewable Energy Laboratory, Golden, Colorado 80401, United States of America
[2]Chemical Sciences and Engineering Division, Argonne National Laboratory, Lemont, Illinois 60439, United States of America
[3]Energy Storage and Electric Transportation Department, Idaho National Laboratory, Idaho Falls, Idaho 83415, United States of America
[4]Materials, Chemical, and Computational Science Directorate, National Renewable Energy Laboratory, Golden, Colorado 80401, United States of America

Battery performance is strongly correlated with electrode microstructure and weight loading of the electrode components. Among them are the carbon-black and binder additives that enhance effective conductivity and provide mechanical integrity. However, these both reduce effective ionic transport in the electrolyte phase and reduce energy density. Therefore, an optimal additive loading is required to maximize performance, especially for fast charging where ionic transport is essential. Such optimization analysis is however challenging due to the nanoscale imaging limitations that prevent characterizing this additive phase and thus quantifying its impact on performance. Herein, an additive-phase generation algorithm has been developed to remedy this limitation and identify percolation threshold used to define a minimal additive loading. Improved ionic transport coefficients from reducing additive loading has been then quantified through homogenization calculation, macroscale model fitting, and experimental symmetric cell measurement, with good agreement between the methods. Rate capability test demonstrates capacity improvement at fast charge at the beginning of life, from 37% to 55%, respectively for high and low additive loading during 6C CC charging, in agreement with macroscale model, and attributed to a combination of lower cathode impedance, reduced electrode tortuosity and cathode thickness.

Lithium-ion battery (LIB) electrodes are porous microstructures, with active material particles blended with conductive additives and binder being the typical solid matrix while an electrolyte solution fills the pores. Cost-effective electrodes that are able to withstand extreme fast charging and high-rate discharge pulses are required features to accelerate the mass deployment of electric vehicles.[1] Among the various approaches investigated to achieve this objective, tailoring the electrode microstructure is a promising avenue to enable fast charging for thick electrodes without inducing significant degradation.[2] Indeed, LIB performance is strongly correlated with electrode microstructures, as seen in previous works.[2–5] LIB macroscale pseudo-2D models based on Doyle and Newmann original formulation[6–8] typically abstract the composite electrode microstructure with five parameters: specific active surface area S_p, mean particle diameter D_{50}, porosity ε, tortuosity factor τ, and solid-phase effective conductivity K_s^{eff}. Carefully tuning the above-mentioned parameters is essential to provide high volumetric energy density (ε), prevent kinetic (S_p) and solid-state diffusion (D_{50}) limitations, lithium-ion transport limitation in the electrolyte (ε, τ) and electronic transport limitation in the solid (K_s^{eff}). While models can help identify desired values for fast charge applications,[2] designing such an ideal electrode is a challenging task due to the limited control on the electrode microstructure manufacturing process, the parameters interdependence[3,9] and intricate entanglement with the electrode microstructure topology and particle morphology.[10]

Of primary interest for fast charging is the electrolyte transport properties,[4,11] notably the effective diffusion coefficient along the thickness (or through-plane) of the electrode, denoted $D_e^{eff,tp}$, that must be high enough to prevent electrolyte transport limitation. During fast charge, insufficient electrolyte diffusion can even lead to electrolyte depletion at the back of the anode (current collector-side), effectively reducing the achievable capacity and overstressing the front of the electrode (separator-side), eventually triggering earlier onset of particular degradation mechanisms such as lithium-plating that can induce capacity fade.[2,4,11,12] This coefficient is correlated with the bulk (i.e., dense) electrolyte diffusion coefficient D_e^{bulk}, the pore tortuosity factor along the thickness of the electrode τ_{pore}^{tp} (which denotes the effect of the convoluted, tortuous, path of the pores that hinders Li-ion diffusion along the considered direction), and the pore volume fraction ε_{pore} (the volume available for the diffusion) according to Eq. 1.[13,14] Alternatively, the Bruggeman exponent along the through-plane direction p_{pore}^{tp} can be used, or the MacMullin number N_M. Reducing the tortuosity of the electrode is therefore one solution considered to enable fast charging.[2,15]

Tortuosity factor has been extensively investigated in the litterature,[16–18] and is a function of electrode design and architecture at the submillimeter scale,[19] porosity, pore topology, and particle morphology at the microstructure scale,[10] and of additive weight and morphology at the nanometer scale.[5,9,20] At the submillimeter scale, electrode structuring through co-extrusion,[21] laser ablation[22,23] or freeze casting[24] can provide secondary pore network channels that significantly improve rate-capability for thick electrodes.[25] At the microstructure scale, material selection,[5,10] calendering (i.e., porosity),[5,26] and magnetic alignment[27] are possible paths to decrease the tortuosity. Unlike for the other scales, few options are available to control the tortuosity at the nanometer scale. The most common approach is to simply reduce the additive weight loading, while keeping it high enough to maintain the solid matrix percolation

*Electrochemical Society Member.
zE-mail: francois.usseglioviretta@nrel.gov

and conductivity. The absence of alternatives is due to the limited manufacturing control at this scale and the limited understanding of shape and spatial distribution of this material (because of imaging limitations[5]), which induce significant uncertainty in modeling. Such uncertainty on the estimation of the tortuosity factor is particularly detrimental on a model's predictivity for fast charge application, as pseudo two-dimensional (P2D) models' sensitivity with tortuosity factor increases with C-rate.[28] Say otherwise, error propagation from tortuosity factor estimation to model prediction is increasing with C-rate. Therefore having an accurate estimation of this parameter is even more important for fast charge modeling. Furthermore, previous work indicated that changes in the tortuosity factor induced by the presence of additives cannot be explained solely by a change of porosity, with additives being more detrimental to the tortuosity than active materials for the same unit volume fraction.[5] Such results indicate that diffusion improvement cannot be extrapolated from a knowledge of only the active material spatial distribution, without additional information or assumptions about the carbon-binder domain (CBD). Both items mentioned above (uncertainty and higher tortuosity penalty) provide a strong incentive to improve modeling of the additive phase and determining its optimal weight loading in order to improve fast charge performance, which is the focus of this work. The next two sections provide a review on LIB additive imaging and modeling, and detail the aim and organization of this present work.

$$\frac{D_e^{eff,tp}}{D_e^{bulk}} = \frac{\varepsilon_{pore}}{\tau_{pore}^{tp}} = \varepsilon_{pore}\, p_{pore}^{tp} = N_M^{-1} \qquad [1]$$

Review of Carbon-Binder Imaging and Modeling

Carbon-binder domain is typically indistinguishable from the pore domain with reconstructed volumes obtained with X-ray Computed Tomography (CT) due to their weak X-ray absorbance resulting in a lack of contrast between the two domains.[5] Therefore, most observations are realized with Scanning Electron Microscopy (SEM) for 2D view,[5,29,30] and with Focused Ion Beam Scanning Electron Microscopy (FIB-SEM) for 3D volumes.[31–33] Spatial distribution can be deceptive if analyzed through 2D SEM imaging, as depending on the perspective, either a rather uniform or a very heterogeneous filling of the pores with the largest pores unfilled can be seen.[29] FIB-SEM imaging reveals the nanoscale structure of the CBD, with nanopores ranging from 5 to 150 nm, a nano porosity of 47% (a lower nano porosity, 27%, has been reported, albeit on a 2D SEM image[30]), and a heterogeneous distribution with also the largest pores unfilled.[31] However, due to the small Field of View (FOV) provided with the FIB-SEM technique, there is no guarantee that this observation is representative of the whole electrode. Micro CT imaging performed on NMC electrodes, although achieved with a limited contrast, also indicate that the CBD is preferentially located near neighboring particles, gluing them together in a connected network, while leaving vacant the largest pores.[30] This statement has been corroborated with cryogenic broad ion beam slope-cutting and scanning electron microscopy,[34] and it has been hypothesized that this distribution is due to particle surface wetting combined with capillary transport during the drying process.[35,36] Recently, combined progress in machine learning-based segmentation and hard X-ray phase contrast nano-tomography have enabled larger FOVs to be imaged with CBD visible,[37] which opens up possibilities for more representative analysis.

Three-dimensional volumes enable calculating the tortuosity factor through homogenization calculation.[26,38,39] As mentioned above, 3D volumes that include CBD are typically obtained with FIB-SEM. Unfortunately, the relatively small FOVs provided with FIB-SEM are typically not enough to provide a representative volume (as defined in Ref. 40) for the active material spatial distribution. To remedy this issue, CBD can be numerically

generated within the complementary volume of the active material imaged with CT, with two methods published in the literature. An energy-based approach where CBD deposition is biased toward either the pre-existing active material network or the pre-deposited new additive phase, through a user-defined parameter ω, providing in its two extreme cases a thin CBD layer uniformly deposited at the surface of the active material ($\omega = 0^+$), or a dendritic, web-like CBD structure ($\omega = 1^-$).[9] Alternatively, a level-set based approach also exists, which effectively generates bridges of CBD near adjacent particles.[35] While these approaches differ locally, they both tend to leave the largest pores unfilled,[20] in agreement with experimental observations. Uniform deposition provides the smallest increase in tortuosity, while dendritic ($\omega = 1^-$) and bridge structures both provide the highest increase with similar values obtained for the two methods.[5,20] Another approach consists in modeling the manufacturing steps, from slurry equilibration to calendering. Different numerical methods have been investigated in the literature, coarse-grained molecular dynamics (CGMD) and discrete element method (DEM) for A. Franco's group,[41,42] multi-phase smoothed particle (MSMP) for D. Wheeler's group[43,44] and DEM for S. Roberts' group.[45] The drying mechanisms, partly responsible for binder migration,[35,36] are however not fully understood yet[44] which may result in some uncertainty in the actual CBD spatial distribution.

Aim and organization of the article.—CBD impact on LIB performance is two-fold. Binder glues together all active material particles in a cluster connected to the current collector foil, preventing electronically isolated particles and thus inert materials, and carbon black improves effective conductivity. However, CBD is an obstacle for the lithium-ion transport within the electrolyte thus penalizing their effective diffusion. The CBD impact on effective conductivity is expected to be either incremental or binary (all or nothing), respectively, for similar, or orders of magnitude different bulk conductivity between the active material and the CBD. In the first case, calculating the effective solid conductivity through a homogenization calculation is required to determine the incremental variations. In the latter case, only calculating the percolation threshold (as defined later in the *Numerical methods* section) is needed, as there are no electrical conduction limitations when enough CBD is present to connect the particles to the current collector. Conversely, if there is not enough CBD, conduction may become limiting due to poor active material conduction compared with the CBD.[35] In regards with the CBD impact on effective electrolyte diffusion, pore percolation is not an issue as seen in previous work[5] (besides, CBD being porous[31] does not entirely block pathways), and therefore homogenization calculation is required.

In this work, solid percolation threshold, solid effective conductivity, and electrolyte effective diffusivity are calculated. The first two parameters are used to identify the optimal CBD weight loading, required to provide high enough conductivity/percolation thus offering minimal penalty on the effective ionic diffusion. The third parameter is used to predict the impact of a CBD loading change, from a baseline loading to this optimal loading (denoted as CBD-optimized cell) on the electrolyte transport. A P2D model from a previous work[46] is then utilized to estimate the performance improvement at various rates, and model results are compared with experimental measurements. The *Numerical methods* section details the CBD transport estimation, based on a reverse homogenization approach, i.e., deducing the nanoscale coefficient from a knowledge of the macro and microstructure scale transport coefficients. Two cases are considered: a uniform and a heterogeneous CBD distribution. For the latter CBD is numerically generated by a newly developed algorithm, also presented in this section. Percolation and effective solid conductivity calculations on the three-phase volume are introduced, as well. The P2D model is briefly summarized with a focus on the treatment of the transport properties. The *Experimental measurements* section details the methodology used to validate the
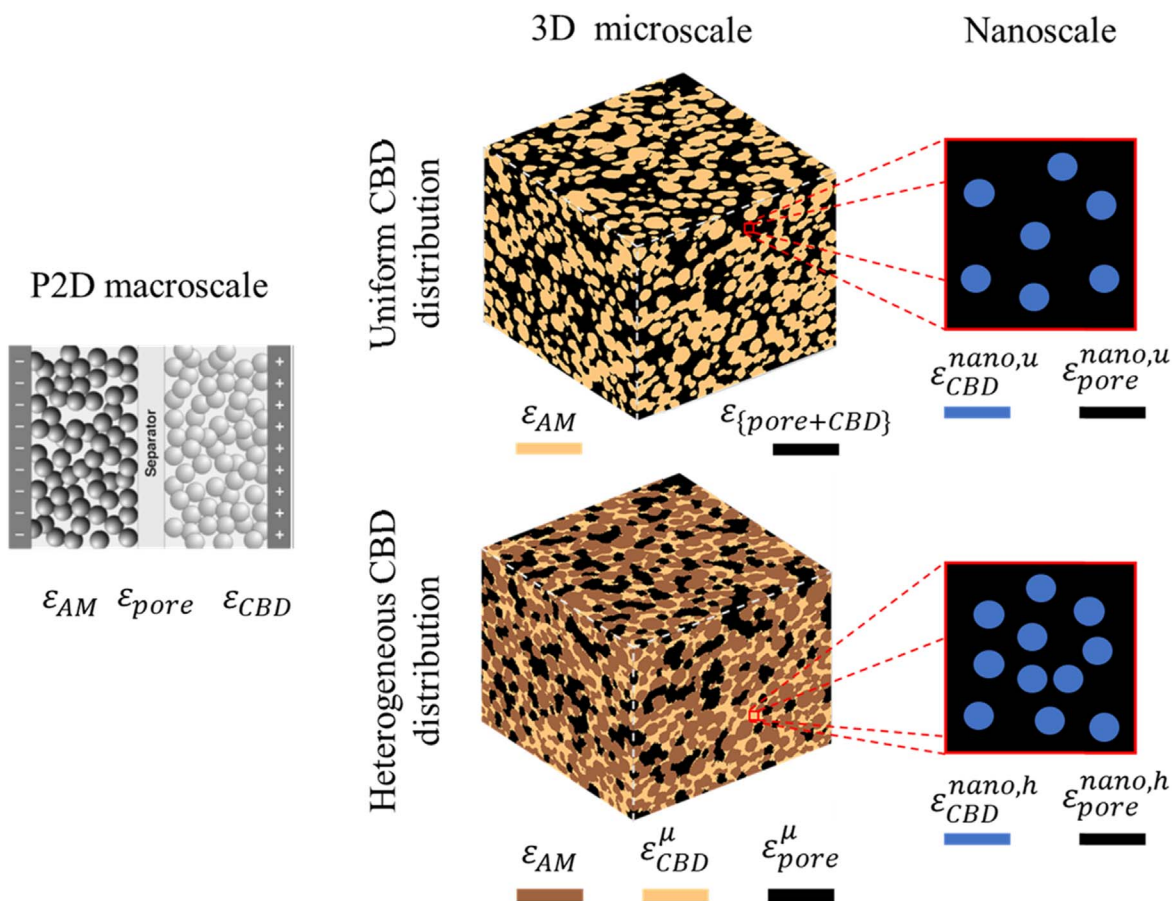
Figure 1. Volume fractions at macro-, micro-, and nanoscale. Uniform (top row) and heterogeneous (bottom row) CBD distribution within the active material complementary volume, resulting in different nanoporosity. Illustrated for an NMC electrode.

model parameter estimation and refine the model result interpretation closes this section. The *Electrode library* section presents the electrodes investigated in this work, with coin and pouch cells fabricated with baseline and optimal amount of CBD, along with the challenges associated in reducing the CBD content. The *Results* section is divided into two subsections. *Microstructure analysis* provides the optimal CBD weight threshold and the associated expected transport improvement. *Cell performance* delivers cell voltage and lithium plating model's prediction for both baseline and CBD-optimized cell, with cell voltage experimentally verified. CBD-optimized cells show significant improvements in high-rate charge acceptance and a reduction in lithium plating. In addition, tortuosity and impedance measurements also provide additional insights on the performance improvements. *Discussion* and *Conclusion* sections complete the article.

Numerical Methods

In this work, no difference is made between binder and carbon-black additive materials, therefore CBD refers to a mixed phase. Three metrics are investigated: the nanoscale CBD Bruggeman exponent, the solid network percolation, and the effective solid conductivity. Determining the nanoscale CBD Bruggeman exponent enables us to discriminate the impact of the active material loading and of the CBD loading on the macroscale electrolyte transport property. This allows us to predict the macroscale electrolyte transport property for a given active material loading but at variable CBD loading, as done in this work. By comparison, macroscale-based estimation either through fitting or experimental measurements cannot deconvolute the impact of the two scales, i.e., microstructure scale (active material) and nanoscale (CBD) for a

composite active material/CBD electrode. CBD transport coefficient can nevertheless be determined through nanoscale imaging focused only on the CBD[31] (albeit with a very limited field of view and thus possible representativity issue), and direct experimental measurement performed on a CBD film.[47] CBD transport properties calculated in this work will be compared with the literature. Determining the other two parameters allows us to identify an optimal CBD loading for the manufacturing process, for which the expected transport improvement is deduced by using the nanoscale CBD Bruggeman exponent.

CBD electrolyte transport property estimation.—*Nanoscale transport coefficient estimated through reverse homogenization.*—Two approaches are considered and illustrated in Fig. 1. Either the CBD is assumed to fill uniformly the active material complementary domain {pore + CBD}, or the CBD is assumed to be preferentially located between neighboring particles. The second approach is supported by various imaging measurements, as discussed in the introduction. However, it requires a 3D map of the CBD location, in this work numerically generated with an original algorithm presented later in this section. The first approach neglects the impact of CBD spatial heterogeneity but is otherwise much faster. Both approaches assume the effective (i.e., macroscale) electrolyte transport coefficient ($X_e^{eff, tp}$, with $X = D \ or \ K$, respectively for diffusivity and conductivity) is known (either from fitting, as done in this work, or from experimental measurements), and that the active material microstructure is known for a volume large enough to be representative (in this work, from CT imaging). The method is called reverse homogenization, as we use macro- and micro- scale transport coefficients to deduce the nanoscale one, that is, from higher scale to

Table I. Relationships between the volume fractions ε at different scales. In the uniform CBD distribution, $\varepsilon_{pore}^{nano,u}$ is the unknown, while in the heterogeneous CBD distribution $\varepsilon_{pore}^{nano,h}$ is known from imaging and ε_{pore}^{μ} and ε_{CBD}^{μ} are the unknowns. Upper script specifies the scale (*nano* for nanoscale, μ for microstructure scale, and macroscale if not indicated) and the CBD representation (*u* for uniform, *h* for heterogeneous), and bottom script specifies the domain.

Macroscale, recipe		$\boldsymbol{\varepsilon_{AM} + \varepsilon_{pore} + \varepsilon_{CBD} = 1}$	[2]
Uniform CBD distribution	Microstructure scale	$\varepsilon_{\{pore+CBD\}} = \varepsilon_{pore} + \varepsilon_{CBD}$	[3a]
	Nanoscale	$\varepsilon_{pore} = \varepsilon_{pore}^{nano,u}\varepsilon_{\{pore+CBD\}}$	[3b]
		$\varepsilon_{pore}^{nano,u} + \varepsilon_{CBD}^{nano,u} = 1$	[3c]
Heterogeneous CBD distribution	Microstructure scale	$\varepsilon_{AM} + \varepsilon_{pore}^{\mu} + \varepsilon_{CBD}^{\mu} = 1$	[4a]
	Nanoscale	$\varepsilon_{CBD} = \varepsilon_{CBD}^{nano,h}\varepsilon_{CBD}^{\mu}$	[4b]
		$\varepsilon_{pore}^{nano,h} + \varepsilon_{CBD}^{nano,h} = 1$	[4c]

Table II. Relationships between effective diffusivity and conductivity at different scales. In the uniform CBD distribution, $p^{nano,u}$ is the unknown and is determining by combining Eqs. 5a and 5b (i.e., using Eq. 5c). In the heterogeneous CBD distribution, $p^{nano,h}$ is the unknown and is determined iteratively. $X_{\{pore+CBD\}}^{\mu}$ and X_{CBD}^{μ} are assumed to be isotropic as CBD particles are assumed to be spherical (no preferential directions). *No analytical relationship for the normalized effective transport coefficient of a three-phases materials.

Uniform CBD distribution	Macro ↔ micro scale bridge	$\dfrac{X_e^{eff,tp}}{X_{\{pore+CBD\}}^{\mu}} = \dfrac{\varepsilon_{\{pore+CBD\}}}{\tau_{\{pore+CBD\}}} = \varepsilon_{\{pore+CBD\}}{}^{p_{\{pore+CBD\}}}$	[5a]
	Micro ↔ nano scale bridge	$\dfrac{X_{\{pore+CBD\}}^{\mu}}{X_e^{bulk}} = \dfrac{\varepsilon_{pore}^{nano,u}}{\tau^{nano,u}} = \varepsilon_{pore}^{nano,u p^{nano,u}}$	[5b]
	Macro ↔ micro ↔ nano scale bridge	$\dfrac{X_e^{eff,tp}}{X_e^{bulk}} = \dfrac{\varepsilon_{pore}}{\tau_{pore}} = \varepsilon_{\{pore+CBD\}}{}^{p_{\{pore+CBD\}}}\varepsilon_{pore}^{nano,u p^{nano,u}}$	[5c]
Heterogeneous CBD distribution	Macro ↔ micro scale bridge	*	
	Micro ↔ nano scale bridge	$\dfrac{X_{CBD}^{\mu}}{X_e^{bulk}} = \dfrac{\varepsilon_{pore}^{nano,h}}{\tau^{nano,h}} = \varepsilon_{pore}^{nano,h p^{nano,h}}$	[6]
	Macro ↔ micro ↔ nano scale bridge	*	

lower scale. Tables I and II list the different relationships (Eqs. 2–6) and terms used at different scales, respectively for volume fractions and tortuosities/Bruggeman coefficients. Homogenization calculations are performed using the open-source TauFactor software.[39] Results from both approaches are compared later.

If CBD is uniformly distributed within the pore, then its nanoscale porosity $\varepsilon_{pore}^{nano,u}$ is deduced using Eq. 3b. Then a homogenization calculation is performed on the volume imaged with CT, as done in previous work.[5,10,26] However, since CT does not distinguish the CBD from the pore, the parameter calculated is the normalized effective transport coefficient of the combined domain pore with CBD, $X_e^{eff,tp}/X_{\{pore+CBD\}}$ (cf Eq. 5a), instead of the normalized effective transport coefficient of the pore, $X_e^{eff,tp}/X_e^{bulk}$ (cf Eq. 1). A second homogenization is needed on a domain containing only pore and CBD, that requires knowing the previously determined nanoscale porosity $\varepsilon_{pore}^{nano,u}$ and the transport coefficient $\tau^{nano,u}$ or $p^{nano,u}$ (the only remaining unknowns), to determine $X_{\{pore+CBD\}}^{\mu}/X_e^{bulk}$ (cf Eq. 5b) in order to retrieve $X_e^{eff,tp}$ (cf Eq. 5c).

If CBD is heterogeneously distributed within the pore and its nanoscale porosity $\varepsilon_{CBD}^{nano,h}$ is known (in this work, we assume it equal to 47% based on FIB-SEM imaging[31]), then the CBD volume fraction visible at the microstructure scale ε_{CBD}^{μ} can be deduced with Eq. 4b. The CBD is then generated to match this volume fraction. Unlike the first approach, there is no analytical relationship for the normalized effective transport coefficient of a three-phase material, with two conductive phases (pore and effective CBD). Therefore, the effective normalized transport coefficient of the effective CBD phase, X_{CBD}^{μ}/X_e^{bulk}, is fitted iteratively through a three-phase homogenization calculation (pore: $X_e^{bulk} = 1$, CBD: X_{CBD}^{μ}/X_e^{bulk} unknown, active material: 0) until $X_e^{eff,tp}$ is matched. Once X_{CBD}^{μ}/X_e^{bulk} has been established, $p^{nano,h}$ can be retrieved using Eq. 6.

Solid matrix percolation and effective conductivity calculation.—This section is only relevant for heterogeneous CBD distributions. LIB electrode volumes obtained from CT imaging typically do not represent the active material domain as isolated particles, but rather as a unique connected cluster[5,10] (cf Fig. 2, left). This prevents the identification of the connectivity category of the active material (as defined in the subsequent *percolation analysis* paragraph, cf Fig. 3 right). I.e., discriminating active materials that are connected to the current connector through CBD (high effective conductivity), or through a series of CBD and active material particles (poor effective conductivity). Furthermore, the active material cluster as seen typically in CT is nearly 100% connected while the individual particles within are actually isolated and need CBD to be connected as seen in SEM and FIB-SEM imaging.[5,29–33] Therefore, CT imaging introduces a bias in connectivity analysis. To remedy it, particles are first labelled, and particle-to-particle interfaces are assigned to the pore domain, effectively isolating particles. CBD is then generated within the pore domain. Lastly, percolation and solid effective conductivity are calculated. Subsequent paragraphs detail the above-mentioned steps.

Particle identification and particle-particle interface removal.— Particles are identified (labelled) using a particle identification algorithm, Pseudo-Coulomb Repulsive Field (PCRF), introduced in a previous work.[10] PCRF consists of dropping charged points between a fixed domain's boundary also charged with the same polarity and identifying particles based on the trajectory of these charged points according to a pseudo-Coulomb's law. Compared with baseline watershed, this method is less sensitive to surface roughness and therefore exhibits less oversegmentation.[10] Due to the high CPU-cost associated with this method, the 3D volume is first downscaled before particle identification. Once particles are labelled, voxels located at the interface between two adjacent particles are removed (cf Fig. 2). Therefore, a 2-voxel-length separation is introduced between particles (cf Fig. 2 middle, white region) that CBD will later fill. The separation length is then function of the image resolution, which introduced a bias in the analysis. Therefore, to estimate the impact of the separation region width on the solid percolation and conductivity (as a thinner width implies more CBD
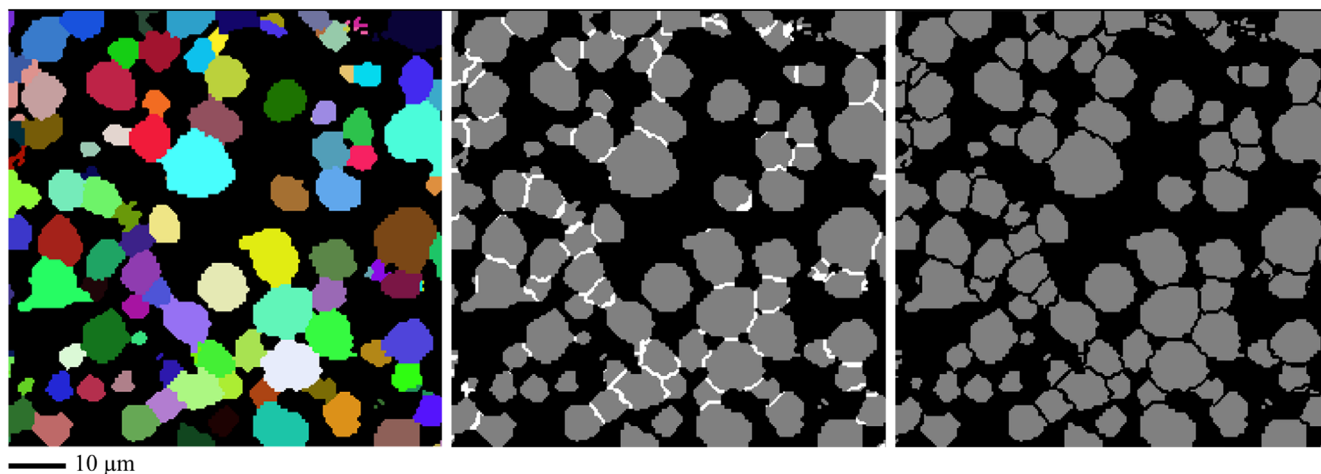
Figure 2. (Left) Particle identification with random color assigned for each labelled particle. Particles are nearly all connected to the same cluster. (middle) Connections between particles are marked (white pixels), and (right) assigned to the pore domain so that particles are no longer in contact. Illustrated for an NMC electrode with a 300 nm voxel length (separation width = 600 nm). Algorithm is applied on the 3D volume and figure shows only a cross-section of the result.

will be available to fill the larger pores) a second volume is investigated, with the same FOV but with a twice higher resolution. To do so, an upscale step (scaling factor of 2) is applied after particle have been labeled, and then particle-particle interface is removed, which results in a twice thinner separation width (600 nm vs 1200 nm before upscaling). Imaging indicates that the region width between neighboring particles is roughly one micrometer or less,[29,30] therefore our method produced relevant dimensions. Particle identification and scaling have been performed with the NREL Microstructure Analysis Toolbox (MATBOX) open-source toolbox[48] available at.[49] This step is not realized for the evaluation of the effective electrolyte diffusion coefficient, as we neglect the ionic diffusion paths between adjacent particles due to their nanoscale section compared with micrometer-size pores.

Percolation analysis.—One function of the CBD is to glue together active material particles in a cluster in contact with the current collector in order to connect particles to the electric circuit. Therefore, the percolation (or connectivity) analysis is directional (along thickness) and oriented (current collector side). Active material particles are considered connected if they belong to a solid cluster in contact with the current collector side (cf Fig. 3 left: S-CC and CC connected clusters). A cluster is defined as a group of voxels that share at least one face. Unknown and isolated clusters, as defined by Joos et al.,[50] represent particles for which connectivity is unknown due to the limited FOV (i.e., edge effect) and particles not connected to the electric circuit (inert material), respectively (cf. Fig. 3 left: UC unknown and I1, I2 isolated clusters). Clusters are identified with the MATLAB built-in function *bwlabeln* with the connectivity parameter equal to 6 (i.e., face-to-face connection). The function is called in the NREL Microstructure Analysis Toolbox (MATBOX) open-source toolbox[48] available at[49] to get the oriented connectivity. The analysis is oriented toward electrical optimization, with no consideration for mechanical optimization.

The connectivity of the active material that belong to either S-CC or CC clusters can be sorted into four categories, depending on the solid paths available from a given active material particle to the current collector (cf. Fig. 3 right):

I. All available paths go only through active material particles. Effective conductivity of the connected solid cluster is limited by the active material bulk conductivity.

II. Available paths either go through only active material particles (I) or through several active material particles *and* through the CBD connected network. The effective conductivity of the connected solid cluster is limited by the active material bulk

conductivity, as it follows a series' law for which the weaker link (the material with poorest conductivity, i.e., the active material) controls the overall conductivity.[51]

III. Among the available paths, there is at least one that goes directly from the active material particle to the current collector through the CBD connected network without needing to go through another active material particle. Effective conductivity of the connected solid cluster benefits from the high carbon black conductivity.

IV. The active material touches the current collector.

Active materials with poor bulk solid conductivity for which particles belong to categories III and/or IV clusters are *not* expected to be limited by their solid conductivity. Conversely, active materials for which particles belong only to categories I and/or II will be limited by their bulk conductivity. Lastly, materials with high enough conductivity (in the same order of magnitude than the carbon black additive), such as graphite, will be less impacted by the connectivity category. Therefore, an optimal CBD loading for electrical contact is reached when most of active materials particles can be assigned to categories III and/or IV. Identifying category IV clusters is trivial. Category III clusters are obtained by first calculating the CBD S-CC and CC clusters, and then selecting only active material particles in direct contact with these clusters. Connectivity is then deduced by normalizing the volume of the as-identified particles with the total volume of the active material particles.

Solid effective conductivity.—The connectivity analysis is particularly relevant for the case where the active material conductivity is orders of magnitude lower than the CBD conductivity. In such a case, connecting all active material particles to the current collector through the CBD connected network without intermediates is essential (category III). Otherwise, the penalty for electrons to conduct through the active materials is less detrimental and the only connectivity requirement is that all active materials are connected to the current collector without any other constraints. For this case, the impact of CBD on effective conductivity is expected to be more incremental. NMC conductivity varies by several orders of magnitude depending on its lithiation state,[35,52] and thus both the above cases can occur during cycling. Therefore, the effective solid conductivity is also calculated using TauFactor.[39] Tortuosity factor of the solid matrix τ_s^{tp} is deduced modifying Eq. 1 using a rule of mixture for the product of volume fraction and bulk conductivity, and assuming a Bruggeman relationship for the nano to microscale CBD conductivity. The effective diffusion coefficient
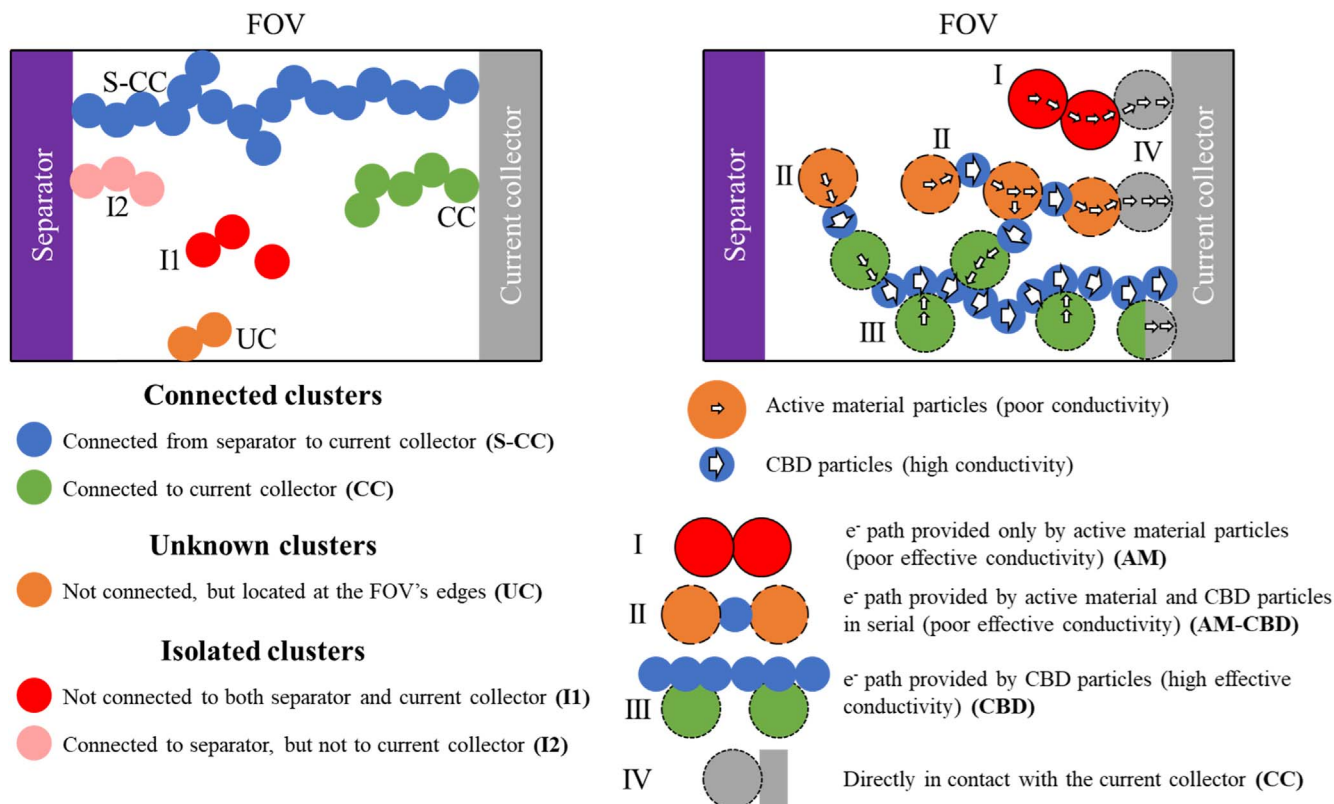
Figure 3. (Left) Cluster connectivity definitions, and (right) electron path categories for the connected clusters.

upper bound (rule of mixture, valid for domain in parallel) is also calculated (cf. Eq. 8) for comparison's sake. The lower bound (inverse rule of mixture, valid for domain in serial) is not relevant in this case as the electrolyte is an electronic insulator (i.e., effective conductivity in series is equal to zero).

$$K_s^{eff,tp} = \frac{\langle K_s^{bulk} \varepsilon_s \rangle}{\tau_s^{tp}} \text{ with } \begin{cases} \langle K_s^{bulk} \varepsilon_s \rangle = K_{NMC}^{bulk} \varepsilon_{NMC} + K_{CBD}^{\mu} \varepsilon_{CBD}^{\mu} \\ K_{CBD}^{\mu} = K_{CBD}^{bulk} \varepsilon_{CBD}^{nano,h1.5} \end{cases}$$

[7]

$$K_s^{eff,mix.} = K_{NMC}^{bulk} \varepsilon_{NMC} + K_{CBD}^{\mu} \varepsilon_{CBD}^{\mu}$$

[8]

Virtual CBD generation.—CBD numerical generation is used for both the effective electrolyte diffusion and the solid percolation and effective conductivity calculations. The algorithm aims to generate CBD phase preferentially between neighbored particles, effectively bridging them together. First, the pore diameters are calculated using the continuum particle size distribution (c-PSD) method.[26,53,54] C-PSD attributes for each voxel of the pore, the diameter of the largest sphere that (i) contains it and (ii) does not overlap with the solid matrix (cf Fig. 4 left). While c-PSD is not recommended to calculate particle size, due to its spherical assumption that strongly underestimates the actual diameter for LIB electrodes as seen in previous work,[10] it otherwise provides a relevant estimation of the distance between neighbored active material particles. Therefore, voxels with a low C-PSD value are likely to be located between neighboring active material particles, which is the desired CBD location in this approach. The CBD generation algorithm then iterates over a distance d, starting at 1-voxel length and increasing with a 1-voxel length increment, marking pore voxels x for which $c\text{-}PSD(x) < d$. If the as-marked voxels are not enough to reach the CBD target volume fraction, then all of them are assigned to the additive phase and d is incremented until the target volume fraction is reached. If too many voxels have

been marked, only a subset of them (cluster-wise) are assigned to the additive phase to match its target volume fraction. Lastly, an erosion step is used to ensure the generated volume exactly matches the target volume fraction. Figure 4 shows CBD generated using this method. Results appear similar to Trembacki et al.[35] level-set based generation algorithm, although methods are different. Algorithm is integrated in the NREL Microstructure Analysis Toolbox (MATBOX) open-source toolbox[48] available at,[49] with full details in the online documentation.

Macroscale lithium-ion battery modeling.—A previously reported macro-homogeneous electrochemical Newman model is used to investigate the effect of lowering CBD content on fast charge performance for moderate loading cells.[2–5,11,55] The graphite/NMC532 active material properties for solid-state diffusion and exchange current density have been previously reported.[2,4] The activation energy for solid-state diffusion and exchange current density are both set to 30 kJ mol^{-1} for both electrodes.[2,4] Based on electrochemical impedance spectroscopy (EIS) measurements, a cathode film resistance of 0.01 Ω-m^2 and 0.008 Ω-m^2 are used for cathodes with 10 wt% CBD and 4 wt% CBD, respectively, with an activation energy of 8 kJ mol^{-1}. A lumped thermal equation is used to calculate internal temperature of a small capacity pouch cell. The heat transfer coefficient is set to 5 W m^{-2} K^{-1}. At normal cycling rates, the cell is estimated to operate nearly iso-thermally. However, at 6C, the cell is estimated to warm by around 3 °C during charging.[2,4] Electrolyte transport properties for Gen2 electrolyte (1.2 M lithium hexafluorophosphate (LiPF$_6$) in 3:7 w-w mix of ethylene carbonate (EC) and ethyl methyl carbonate (EMC) solvent) are a function of local salt concentration and lumped temperature using functional forms previously reported.[2,4]

An important parameter for accurately modeling fast charge is the tortuosity of each electrode and separator. A combination of microstructure modeling and direct electrochemical measurements, such as EIS with blocking electrolyte, have been used to estimate the tortuosity for electrodes with high amount of CBD (8 wt% in anode and 10 wt% in cathode). The anode was found to have a Bruggeman
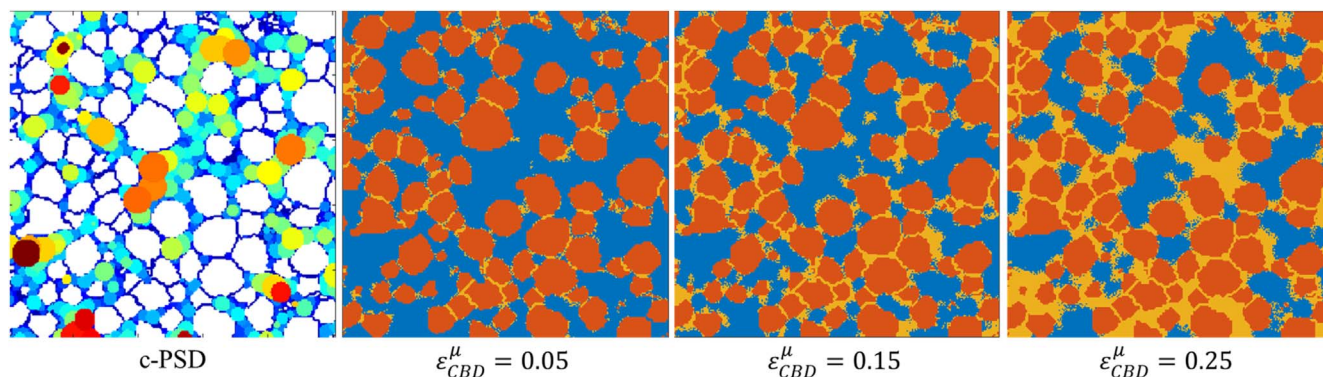
Figure 4. (Left) Pore diameter calculated with c-PSD. (others) Three-phase NMC electrodes with CBD (yellow) numerically generated for different volume fractions. Algorithm is applied on the 3D volume and figure shows only a cross-section of the result.

coefficient of roughly 2.3 and cathode around 2.0, corresponding to tortuosities of 4 and 2.8, respectively, having porosities of ~35%.[4] The 2320 separator tortuosity has been measured by the Gasteiger group to be approximately 4.[56] The tortuosities for electrodes with 4 wt% CBD were estimated using the microstructure modeling tools discussed above. The Bruggeman coefficient for the anode and cathode are predicted to be reduced to around 2 and 1.8, respectively. The thickness of the anode for both CBD contents is 70 microns. However, the cathode with the lower CBD content is 10 microns thinner due to the active material having a significantly higher density than CBD.

Experimental Measurements

Effective ionic transport properties, impedance, and rate capabilities of cell/electrodes with high and low CBD loading (cf. Table III) were measured using different cell configurations with details provided in the subsequent paragraphs.

Tortuosity measurement on symmetric cell.—To validate the microstructure model transport predictions, tortuosity of graphite electrodes was measured using an EIS method previously reported by Landesfeind et al.[56] Two electrodes with varying CBD contents

were examined, with details in the electrode library section (cf Table III). Electrolyte was 10 mM tetrabutylammonium perchlorate (TBAClO$_4$, ⩾99.0%, Sigma-Aldrich) dissolved in EC/EMC (1:1, w/w) (Tomiyama Pure Chemical Industries, Ltd.), which has ionic conductivity of 0.46 mS cm^{-1}.[56] 2032-type coin cells were assembled in an argon (Ar)-filled glove box using two 15 mm diameter graphite electrodes (symmetric cell), 19 mm diameter Celgard 2325 separator, and 120 μl electrolyte. The cells were rested at open circuit voltage for 24 h before the EIS measurement (1 MHz to 0.1 Hz, 10 mV perturbation), which was performed using a BioLogic VMP3 potentiostat at room temperature. From the Nyquist plot, the effective ionic resistance of the electrode (R_{ion}) was determined, and tortuosity was calculated using Eq. 9, where A is the electrode area, K_e^{bulk} is the bulk ionic conductivity of the electrolyte, and d is the electrode thickness. The value is divided by two to account for the symmetric cell configuration.

$$\tau_{pore}^{tp} = \frac{R_{ion} \times A \times K_e^{bulk} \times \varepsilon_{pore}}{2\,d} \quad [9]$$

Impedance measurements in custom 3-electrode cells.—The effect of CBD content on electrode impedance was determined using

Table III. Electrodes experimentally investigated.

			High CBD[57]	Low CBD
Anode (graphite)	Components (wt%)	Superior Graphite SLC1506T	91.83	95.83
		Timcal C45 carbon	2	0.5
		Kureha 9300 PVDF	6	3.5
		oxalic acid	0.17	0.17
	Porosity (%)		38.2	37.4
	Coating loading (mg cm^{-2})		9.38	9.57
	Coating density (g cm^{-3})		1.34	1.37
	Coating thickness (μm)		70	70
	Cu foil thickness (μm)		10	10
	Total electrode thickness (μm)		80	80
	Areal capacity (mAh cm^{-2})	Reversible C/10; 0.005 to 1.5 V vs Li/Li$^+$	2.98	3.05
Cathode (NMC532)	Components (wt%)	Toda NMC532	90	96
		Timcal C45 carbon	5	2
		Solvay Solef 5130 PVDF	5	2
	Porosity (%)		35.6	34.9
	Coating loading (mg cm^{-2})		18.57	17.24
	Coating density (g cm^{-3})		2.62	2.87
	Coating thickness (μm)		71	60
	Al foil thickness (μm)		20	20
	Total electrode thickness (μm)		91	80
	Areal capacity (mAh cm^{-2})	Reversible C/10; 3 to 4.2 V vs Li/Li$^+$	2.54	2.54
Cell	N/P range	3 to 4.1 V	1.04 to 1.17	1.10 to 1.20

custom-made 3-electrode cells. These cells contained 20.3 cm² cathode and anode separated by two sheets of Celgard 2320 and 1.2 ml of Gen2 electrolyte. A 25 μm insulated copper wire was placed in between the separator sheets, with a ~2-mm exposed tip positioned at the center of the electrode stack. A small amount of Li was plated onto the wire in situ to create a reference electrode. This placement of the reference with respect to cathode and anode is essential to improve accuracy and avoid artifacts in the sensed electrode potentials and measured impedance.[58,59] Area-specific impedance (ASI) was measured using a modified version of the hybrid pulse power characterization (HPPC) test. In this experiment, a fully charged cell is discharged in increments of 10% of its total capacity. At each stop, 10-s long 3C discharge and charge pulses are applied, each followed by 40 s of rest. The voltage increment during the pulse at a known current value is used to calculate an impedance value; the calculated ASI for the cathode, anode and cell are presented as a function of full-cell voltage. In addition, the cells were also characterized using EIS at a full-cell voltage of 3.9 V, using 5 mV amplitude between 100 kHz and 10 mHz. Separate spectra were collected to capture the behavior of the full-cell, cathode and anode.

Full cell rate capability screening in coin cells.—Eventually, the main point of reducing CBD loading is to improve capacity at fast charge. To evaluate the performance gain, the rate capability of electrodes containing different CBD content was then evaluated using 2032-format cells. Full-cells were assembled using 1.4 cm and 1.5 cm cathode and anode discs, respectively. The data presented here only pertains to cells in which both electrodes have either high or low CBD content (cf Table III). A 1.6 cm disc of Celgard 2320 was used as the separator. Each cell contained 40 μl of Gen2 electrolyte, which is ~4x the total pore volume of the electrodes and separator. Cells were initial conditioned by performing several constant current cycles at slow rates (<C/5) using 3 V and 4.1 V as cutoffs. Cells were then charged at various rates (up to 6C) until reaching 4.1 V; in case the cutoff was met with charge acceptance below 2.26 mAh cm⁻², cells were held at 4.1 V until this capacity was achieved. Discharge was always performed at C/5, followed by a hold at 3 V until the measured current became smaller than C/100. For ease of comparison, charging rates were calculated based on 1C = 2.26 mA cm⁻² for all cells; at this current density, fully charged cells with high CBD content will discharge to 3 V in 1 h. Testing was performed using a Maccor 4100 cycler.

Single Layer Pouch cells (SLPCs) rate capability and impedance.—The SLPCs were built using the same materials discussed above and formed at Argonne and then shipped to Idaho National Laboratory (INL) for performance testing. Upon receipt, INL performed beginning of life (BOL) characterization that includes capacity tests at C/20 and C/1 between 3 to 4.1 V and EIS test at 3.9 V. Upon BOL characterization, constant current rate capability test (RCTs) with charging rates between 1 to 6C were performed. During the RCTs, cells were charged at a particular C-rate up to 4.1 V that follows a 15 min rest. After the rest, cells were discharged at C/2 to 3 V followed by another 15 min rest. This process was repeated for different charging rates up to 6C. Details about cell building, fixturing, testing protocol can be found in Refs. 11, 60.

Electrode Library

Manufactured samples.—All electrodes and pouch cells evaluated in this work were fabricated by the Cell Analysis, Modeling and Prototyping (CAMP) Facility at Argonne National Laboratory in a climate-controlled dry-room with a dew point less than −42 °C (<100 ppm moisture). The electrodes were formulated to investigate the performance of High CBD (Round2) and Low CBD (CBD-optimized) compositions under fast charging conditions, where the anodes and cathodes exhibit areal capacities of ~3.0 and ~2.5 mAh cm⁻², respectfully. The graphite electrodes, consisted of graphite (Superior Graphite SLC1506T), conductive carbon (Timcal C45), polyvinylidene fluoride binder (PVDF, Kureha 9300), and oxalic acid (Sigma Aldrich) on 10 μm copper foil. The NMC532 electrodes consisted of NMC532 (Toda America), conductive carbon (Timcal C45) and PVDF binder (Solvay Solef 5130) on 20 μm aluminum foil. Detailed electrode compositions and properties are provided in Table III. The electrodes were coated using a roll-to-roll reverse comma coater and calendered by a hydraulic-driven roll press, as described in prior work.[61]

Prior to coating the electrodes, the components of each electrode were well dispersed in a slurry using N-methyl-2-pyrrolidone (NMP). The slurries were prepared in a high-shear planetary mixer (Ross PDM-1\2) or a planetary centrifugal mixer (Thinky U.S.A., INC., ARE-310), depending on the slurry size. The High CBD anode and cathode slurries achieved desirable flow properties at ~44 and ~59% solids, respectfully. Whereas the Low CBD anode and cathode slurries achieved similar rheological characteristics at ~50 and ~75% solids, respectfully. The increase in solids % for the Low CBD slurries is advantageous for electrode processing (i.e., cost savings, enables higher coating speeds and higher coating loadings), however the Low CBD slurries appeared to be more susceptible to component settling during brief storage than High CBD slurries. If low CBD slurries sat stationary for longer than a few hours, the bottom of the container had a slight increase of viscosity compared to the slurry near the top of the container, observed from a simple spatula feedback. This behavior was not observed for the high CBD slurry when sitting stationary for a similar time period. Further studies are needed to quantify the slurry suspension properties. All electrodes were dried overnight under vacuum at 120 °C prior to use.

Cross sections of high and low CBD cathodes are shown in Fig. 5. Qualitative analysis seems to indicate large pores are CBD-free on the low CBD electrode. Quantitative analysis would however be ill-advised as the images contain material not only from the plane of the cross section but also from planes behind, especially noticeable on the low CBD electrode. In addition, limited field of view (not representative) and image quality prevent more in-depth analysis.

Microstructure analysis parameters.—CBD nanoporosity $\varepsilon_{pore}^{nano,h}$ (47%) is taken from literature (FIB-SEM imaging[31]), as well as CBD and NMC bulk conductivities.[35,52] NMC electronic conductivity is highly dependent with state of lithiation, with values ranging from ~1e⁻² to ~1e⁻⁶ S.cm⁻¹ for Li$_x$Ni$_{0.5}$Mn$_{0.2}$Co$_{0.3}$, respectively, for x = 0.25 and 1.0 at 30°C. As lithium irreversible consumption at the anode during SEI growth prevents NMC to re-lithiate fully in subsequent cycles, the conductivity associated to the lithiated NMC is likely to be between the measured values at x = 0.9 (~5e⁻⁴ S.cm⁻¹) and x = 1.0 (~1e⁻⁶ S.cm⁻¹) depending on the severity of the SEI growth. Due to the wide range of NMC conductivity, the effective solid conductivity of the solid matrix has been calculated for the two extreme bounds (1e⁻² and 5e⁻⁴−1e⁻⁶). CBD conductivity is dependent with volume strain, but unlike for NMC, values are much more narrowed, ranging from ~0.02 to ~0.3 S.cm⁻¹ [35](a median value 0.15 S.cm⁻¹ is used in this work). Microstructure volumes imaged in previous works[5,10] with X-ray CT have been re-used. FOVs used for effective ionic diffusion calculations are ~240 × 240 × 127 μm³ and ~115 × 115 × 115 μm³, respectively for NMC532 and graphite. A smaller volume, ~75 × 75 × 75 μm³ (cf Figs. 2, 4), has been used for effective conductivity and percolation analysis for the cathode, due to high CPU-cost associated with the particle identification numerical method.

Results

Microstructure analysis.— *Representativity.*—Representative volume element (RVE) analysis (as done in previous work[26]) was performed with NREL Microstructure Analysis Toolbox (MATBOX) open-source toolbox[48] available at[49] on both electrodes to check the representativity of the volumes investigated. The RVE size were found equal to ~45 × 45 × 45 μm³ and ~14 × 14 × 14 μm³ for volume
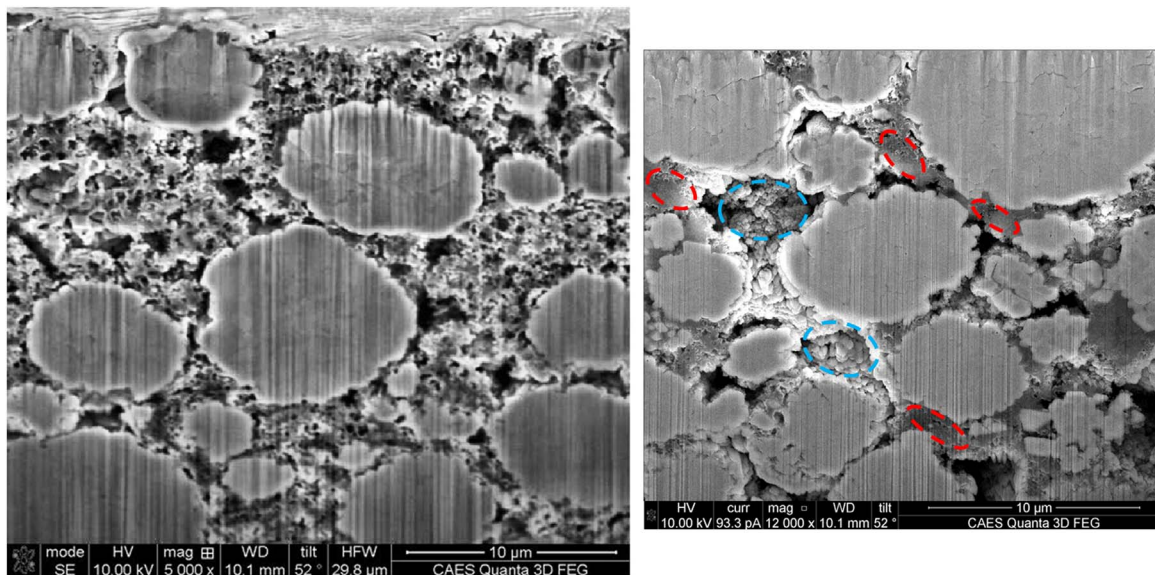
Figure 5. SEM cross section of (Left) high and (right) low CBD cathodes. Dashed circles indicate (blue) large CBD-free pores and (red) CBD binding neighboring particles.

fractions, and $\sim 52 \times 52 \times 52 \ \mu m^3$ and $\sim 42 \times 42 \times 42 \ \mu m^3$ for tortuosity factor, respectively for the cathode and the anode, using a 5% relative standard deviation threshold. RVE sizes being significantly smaller than the investigated volumes, the representativity analysis increases confidence in the characterization/homogenization results of this section.

CBD percolation threshold and effective conductivity.— Connectivity analysis has been performed on the NMC microstructure and results are illustrated in Fig. 6. Isolated and unknown clusters (cf. Fig. 3) of the NMC ∪ CBD domain represents, respectively, only 0.3%–0.5% and 0%–2.6% of the combined domain depending on the CBD loading. The low values indicates that nearly all particles are connected to the current collector: I ∪ II ∪ III ∪ IV connectivity of the NMC active material particles ranges from ~97% to near 100%, whatever the CBD loading (cf Fig. 6, blue dots). The second value indicates a small edge effect impact, suggesting a volume large enough for the analysis, as also indicated by the representativity analysis. Category I and IV connectivity are overlapping (~5.4%), as pre-processing effectively isolated the particles (cf Fig. 2). Therefore, the difference between I ∪ II ∪ III ∪ IV and II ∪ III connectivities indicates the category II connectivity. CBD connectivity (S-CC ∪ CC) is a good indicator of the NMC connectivity (III ∪ IV), cf Fig. 6. This means that achieving percolation for the CBD is synonymous with achieving the desired connectivity for the NMC particles. The percolation transition region for the NMC particles, defined as the 20%–80% III ∪ IV connectivity, is $0.028 \leqslant \varepsilon_{CBD} \leqslant 0.039$ and $0.041 \leqslant \varepsilon_{CBD} \leqslant 0.058$, respectively, for a thin (600 nm width) and a wide (1200 nm width) separation region. Imaging indicates the wide separation is likely to be an upper bound, therefore the $0.041 \leqslant \varepsilon_{CBD} \leqslant 0.058$ is an overestimation of the actual threshold. The baseline volume fraction (0.138) is then unnecessarily high to achieve the percolation objective. The optimal CBD volume fraction is set within the upper range of the percolation threshold to be conservative, at $\varepsilon_{CBD} \approx 0.052$, that corresponds to a CBD weight ratio of 4% (recipe calculation) and ~4.22% (FOV). The small difference between the two values is due to the small amount of active material removed to effectively isolate particles (cf Fig. 2) and is therefore increasing with the separation region width (cf Fig. 6). A lower value (e.g., ~3.1 wt%) just above the thin separation region, while relevant for the pristine electrode, was not selected to keep a security margin especially considering delamination.

The impact of the CBD loading on the solid matrix effective conductivity and tortuosity is plotted in Fig. 7, considering different NMC bulk conductivity for low (SOC = 0.25) and high lithiation (SOC = 0.9 and 1.0). For the low NMC bulk conductivity, the sharpest variation is concomitant with the percolation threshold identified in Fig. 6. Without a percolating CBD network, the effective conductivity is drastically limited by the poor NMC bulk conductivity as expected. Effective conductivity significantly changes from near lithiation (x = 0.9) to fully lithiation (x = 1.0), indicating that, especially for low CBD loading, the effective conductivity of the cathode at the end of discharge is expected to increase during cycling, due to the progressive loss of lithium in the anode side that can prevents full re-lithiation of the cathode. For the high NMC bulk conductivity, the improvement with loading is more incremental, uncorrelated with the percolation transition, and follows the same trend as a rule of mixture (while still being significantly lower than this upper bound). This last result indicates that for active material with high bulk conductivity (e.g., NMC at low lithiation, and graphite), while the CBD contribution on the effective conductivity is still beneficial, achieving III ∪ IV percolation is no more an imperative requirement.

Effective transport properties (baseline).—Volume fractions, from recipe calculations are 0.369/0.492/0.139 and 0.330/0.606/0.064 ($\varepsilon_{pore}/\varepsilon_{AM}/\varepsilon_{CBD}$), respectively for the baseline cathode and anode. A normalized effective ionic diffusion coefficient $D_e^{eff, \, tp}/D_e^{bulk}$ of 0.136 and 0.078 is required to match experimental cell voltage with the P2D model, respectively for the cathode and the anode. This corresponds to a Bruggeman exponent p_{pore}^{tp} (cf Eq. 1) equal to 2.0 and 2.3, respectively, for NMC and graphite, similar to previous estimations from both fitting and direct measurements.[2,4,5]

CT imaging provides $\varepsilon_{\{pore+CBD\}}^{P_{\{pore+CBD\}}}$, $0.507^{1.777}$ and $0.407^{1.953}$, respectively, for NMC and graphite. The above Bruggeman exponents correspond to an extrapolation to 0 nm, to take into consideration the quasi-linear dependence with voxel size, spotted in a previous work,[5] to reduce numerical error due to limited image resolution. To do so, volumes have been downscaled several times to establish the correlation. For a uniform distribution of the CBD within the complementary volume of the active material, the CBD nanoporosity $\varepsilon_{pore}^{nano,u}$ can be deduced using Eq. 3b: 0.726 and 0.847, respectively, for NMC and graphite (volume fractions from imaging have been used for the calculations). Such nanoporosities
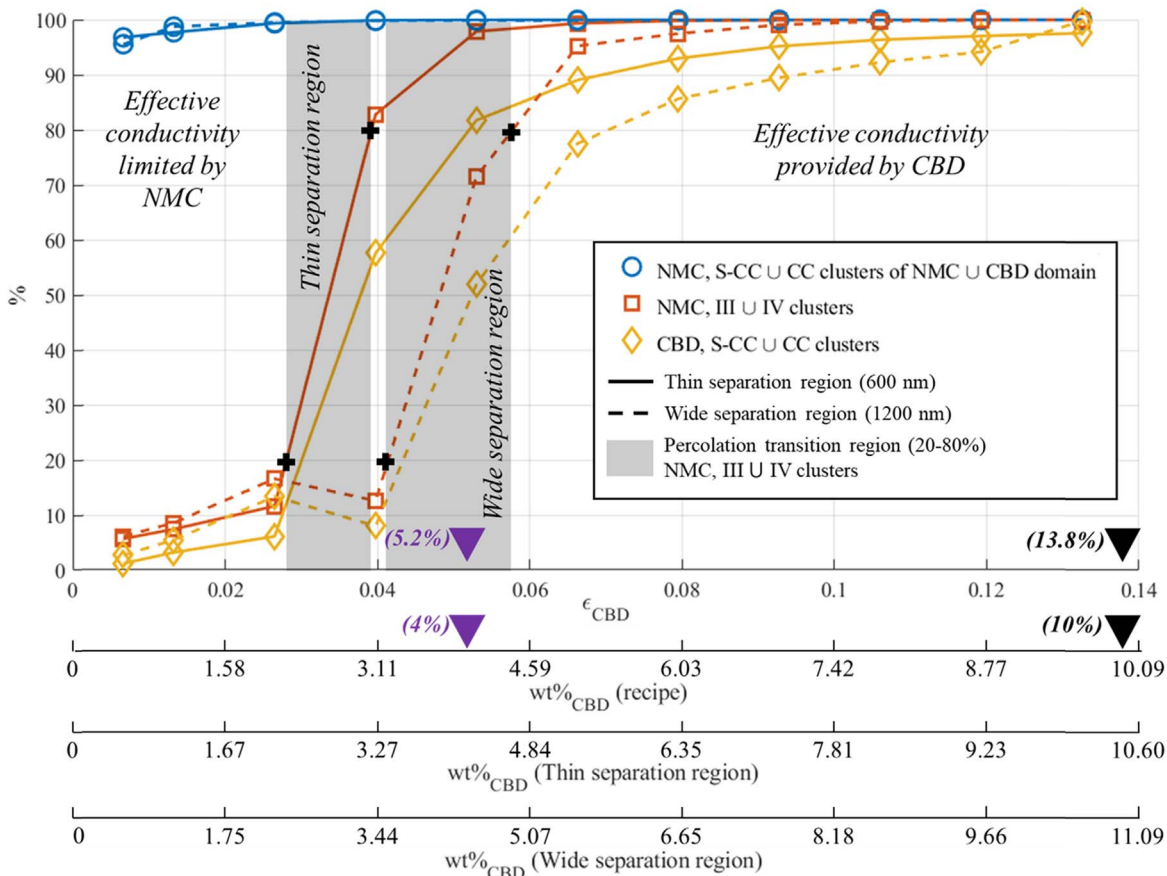
Figure 6. Connectivity of NMC active material that is belonging to S-CC ∪ CC clusters for all categories (I ∪ II ∪ III ∪ IV) (circle), and that is belonging to III ∪ IV clusters (square). CBD connectivity for S-CC ∪ CC clusters is also indicated (diamond). Percolation analysis performed for two separation region width, with CBD weight ratio modified as NMC material is slightly removed. Baseline NMC is marked with a black triangle, CBD-optimized cell is marked with a magenta triangle. Percolation transition regions bounds are marked with thick + symbols.

are higher than the values obtained from imaging (0.47[31]), thus indicating that the uniform distribution assumption is an over-simplification that results in an overfitting of the nanoporosity. The nanoscale Bruggeman exponent $p^{nano,u}$ is then deduced using Eq. 5c: 2.46 and 4.78, respectively for NMC and graphite. The large values calculated are only relevant when associated with the high nanoporosity.

For a heterogeneous distribution of the CBD within the complementary volume of the active material, and assuming a nanoporosity $\varepsilon_{pore}^{nano,h}$ of 0.47, the apparent CBD volume at the microstructure scale ε_{CBD}^{μ} is deduced using Eq. 4b: 0.261 and 0.117, respectively for NMC and graphite. The normalized effective diffusion coefficient of the CBD at the microstructure scale $X_{CBD}^{\mu}/X_{e}^{bulk}$ (cf Eq. 6) is then fitted and resulted in 0.280 and 0.139, respectively for NMC and graphite, so that $X_{e}^{eff,\,tp}/X_{e}^{bulk}$ matches the expected value. As done for the {pore+CBD} combined domain, these values have been extrapolated for a 0 nm voxel size, though downscaling, to take into consideration the image resolution dependence and thus reducing the numerical error. It corresponds to a CBD tortuosity $\tau^{nano,h}$ and Bruggeman exponent $p^{nano,h}$ of 1.67 and 1.68, and 3.37 and 2.61, respectively for NMC and graphite. These values are lower than for the uniform distribution case to balance for the higher density. FIB-SEM nanoscale imaging on CBD from Zielke et al.[31] determined a similar Bruggeman exponent for an NMC electrode (1.81, $X_{CBD}^{\mu}/X_{e}^{bulk} = 0.254$, $\varepsilon_{pore}^{nano,h} = 0.47$), although from the analysis of a small FOV. The slight difference could be explained by either or both the FOV and the numerical calculation and extrapolation. Note that CBD diffusivity reported in the literature[47] from direct

measurement provided a much lower value, ~5%. However, measurement was performed on a CBD film, thus not on a CBD as manufactured for electrodes, and for a different carbon black/binder ratio. Furthermore, this ratio has a significant impact on the measured CBD effective transport[47] and thus cannot be used for comparison in this work.

Effective transport properties (CBD-optimized cell).—Three cases are possible: keep the same active material volume fraction but increase porosity, increase active material volume fraction but keep same porosity, and lastly any other volumes fractions combination as long as it corresponds to a 4%wt CBD. The first case is particularly interesting as it allows comparing the uniform and heterogeneous CBD distribution approaches (as the CT volume can be re-used to generate CBD with the reduced loading). The two first cases provide bounds, respectively for maximizing ionic diffusion and maximizing theoretical capacity from the same baseline. The last case corresponds to the manufactured cell having a reduced loading, but that slightly differs from one of the two above-mentioned cases. Lower scale Bruggeman coefficients ($p^{nano,u}$, $p^{nano,h}$) fitted for the baseline are re-used as the CBD topology is assumed to be independent from its loading.

Figure 8 illustrates the results for the cathode. The as-calculated reduction for the Bruggeman exponent (cf Fig. 8a) is due to a change of the CBD nanoporosity for the CBD uniform approach (cf Figs. 8c, 8d) and to a change of the CBD volume fraction and spatial distribution (but with unchanged nanoporosity) for the CBD heterogeneous approach (cf Fig. 4). Once in the reduced CBD loading state, varying porosity does not lead to significant changes in the
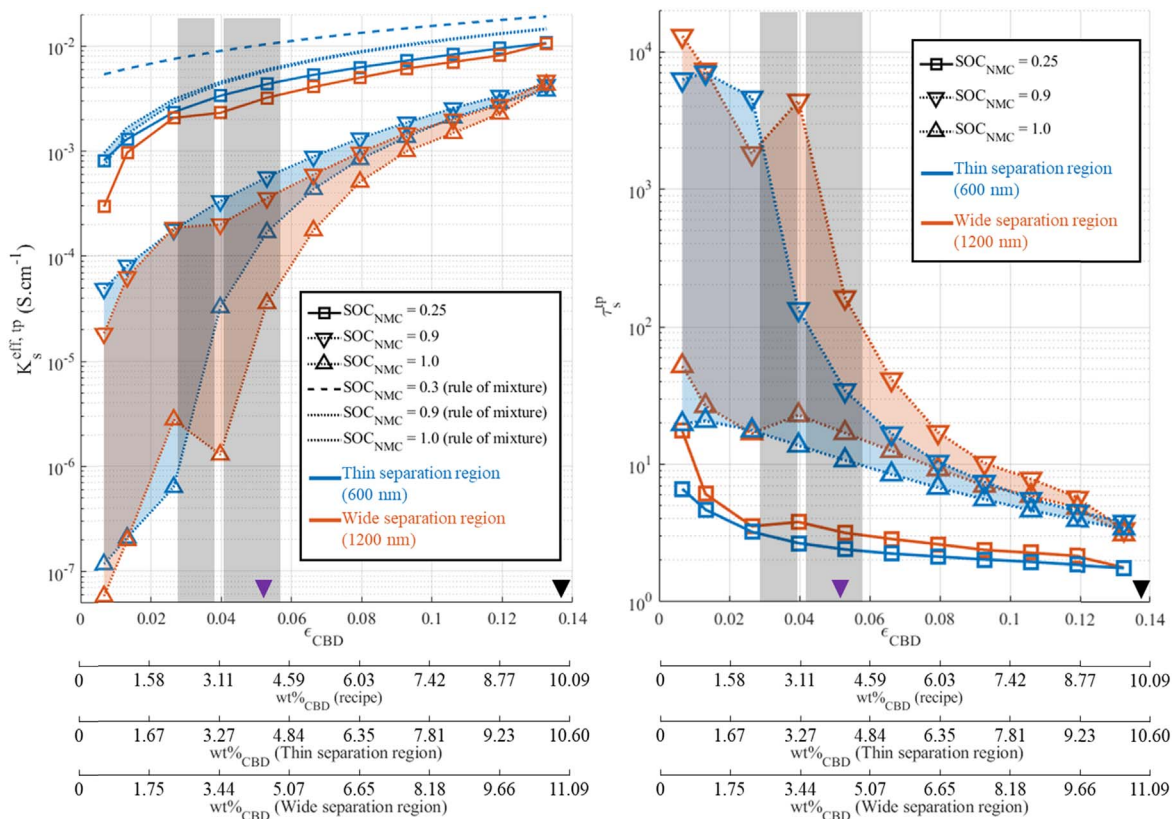
Figure 7. (Left) Effective solid conductivity and (right) associated solid tortuosity factor, considering low lithiation (square) and high lithiation (triangle) NMC532 bulk conductivity. At end of discharge, NMC effective conductivity if likely to be within the transparent area due to lithium loss in the anode. Two cases are investigated thin (blue) and wide (orange) separation regions between adjacent particles (cf Fig. 2). CBD weight loading is slightly impacted as active material loss is different. Dashed lines (left) represent the effective conductivity calculated with a rule of mixture $K_s^{eff,mix.}$ for the different NMC bulk conductivities, but only for the thin separation region to keep figure clear enough. Baseline NMC is marked with a black triangle, CBD-optimized cell is marked with a magenta triangle. Grey vertical area corresponds of the percolation transition region (cf. Fig. 6).

Bruggeman exponent as both particle morphology and lower scale coefficients are nearly constant. Both CBD uniform distribution and heterogeneous distribution cases are equivalent for macroscale properties (cf Fig. 8a). This was enforced for the baseline through fitting so that each approach starts from the same point and can be compared subsequently. However, for the reduced loading (higher porosity, same NMC loading case) the agreement between the uniform and heterogeneous CBD distribution indicates that both approaches are equivalent for the effective parameters, *providing they have been fitting once at the same point*. The relevance of each approach is further debated in the discussion section. The Bruggeman exponent determined with the microstructure approach is ~1.88, while the value used in the P2D model is 1.8 (from a 2.0 baseline). That is the microstructure analysis only explained 60% of the Bruggeman reduction, with possible explanations further debated in the discussion section. The most practical parameter for the LIB application is the normalized effective diffusion coefficient. The CBD loading reduction allowed for an improvement, even though the porosity is reduced (cf Fig. 8b), which demonstrates that the CBD impact on the effective transport is more detrimental compared with NMC for the same volume fraction. Figure 8b also indicates the error performed if the effective transport coefficient would have been determined simply by re-using the baseline Bruggeman exponent (p = cst cases) with the modified porosity. The minor error, while insignificant for low C-rates, can bias the model prediction at higher C-rates as error propagation is increasing with the applied current.[28] Similar trends have been calculated for the graphite, with a Bruggeman coefficient reduction from 2.39 to 2.10 (difference with P2D baseline 2.3 being due to minor difference in

volume fractions from recipe calculation). Bruggeman macroscale coefficients are listed in Table IV.

Interface area.—Specific interface area between NMC and CBD have been also calculated on the 3D volume with values equal to 0.2173 μm^{-1} and 0.1615 μm^{-1}, respectively, for the baseline and the CBD-optimized cathodes. A simple face summation method has been utilized with a 2/3 corrective factor to account for the voxel discretization of the medium.[26,62] The absolute values must be considered with caution, as interface area deduced from 3D reconstructed volumes are strongly dependent on the voxel size, as discussed in a previous work.[10] However, relative variation calculated between electrodes investigated at the same image resolution are relevant. In this case, a 25% reduction to be compared with the 20% reduction on the cathode film resistance measured with EIS, which is attributed to the NMC surface blocked by CBD. Such good agreement, assuming proportionality between cathode film resistance and CBD-NMC contact area, supports the experimental measurement in addition to provide an indirect validation of the CBD generation algorithm.

The CBD loading reduction led to an increase of the active material—electrolyte specific surface area, from 0.145 to 0.174 μm^{-1} (~+20%) and from 0.701 to 0.791 μm^{-1} (+~13%), respectively, for the cathode and the anode. Element of surface between active material and CBD are counted but scaled down to 47% of their value to reflect the CBD nanoporosity. The absolute values reported here are not to be considered true, as dependence with surface roughness (i.e., with voxel size) is not considered, and out of the scope of this work. Interface areas have been nevertheless
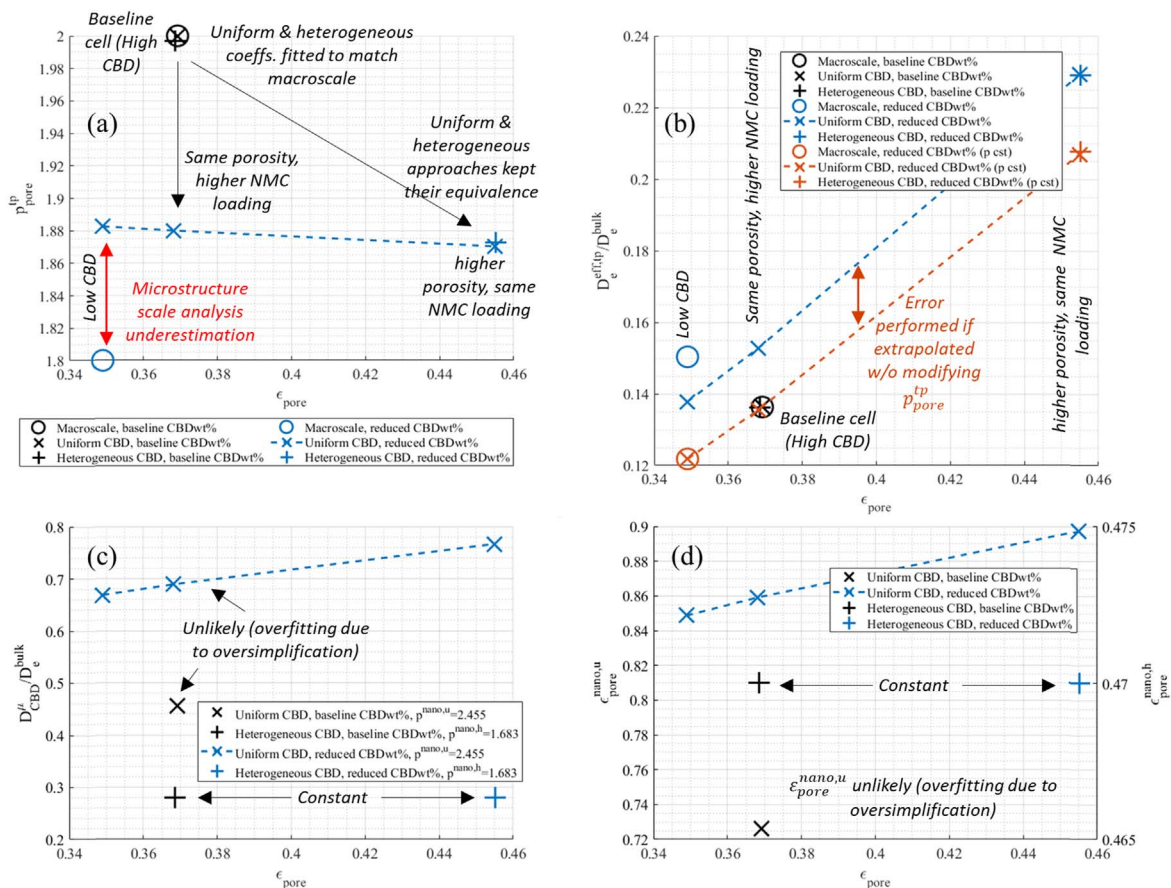
Figure 8. (Top) Effective transport coefficient: (a) Bruggeman exponent and (b) normalized effective diffusion coefficient. "Macroscale" here refers to the values used in the P2D macroscale model to fit electrochemical data. (Bottom) Associated lower scale coefficient: (c) CBD normalized microstructure scale diffusion coefficient and (d) CBD nanoporosity. Results correspond to the NMC electrode.

calculated at the same voxel size (398 nm) for both volumes to enable comparison. However, the relative evolution is believed to be accurate as surface roughness is unchanged between the low and high CBD loading. Particle diameters (independent from CBD loading) have been investigated in a previous work.[10]

Cell performance.— *Tortuosity experimental measurement and model predictions.*—Nyquist plots of the graphite/graphite symmetric coin cells are shown in Fig. 9. R_{ion} values were calculated using $R_h - R_l \approx R_{ion}/3$ approximation, where R_h and R_l are the x-intercept of high and low frequency region slopes, respectively.[63] The measurement was repeated twice for each electrode and the results were reproduced: $R_{ion,HighCBD}$ = 186 and 185 Ω; $R_{ion,LowCBD}$ = 143 and 137 Ω. Tortuosity of the two electrodes calculated using these R_{ion} values have been then deduced using Eq. 9, with values listed in Table IV. Experimental results demonstrate that reducing the carbon binder loading lead to much improved ionic transport property (N_M decreases by ~25%), even while porosity is slightly reduced. Such counter-intuitive result, improving ionic diffusion by reducing porosity, is due to the non-equivalence between a unit volume of active material and a unit volume of CBD for their respective impact on the effective transport, as seen also for the cathode (cf Fig. 8b). The most relevant parameter for comparing the three methods reported in Table IV is the Bruggeman exponent p_{pore}^{tp} as this coefficient is not, or very little, dependent with the porosity, unlike τ_{pore}^{tp} and N_M. Both methods show good agreement, with ~13% Bruggeman reduction induced by the CBD loading reduction. No values are reported for the cathode as aluminum positive current collector interferes with the blocking condition needed for the measurement, while cupper negative current collector does not
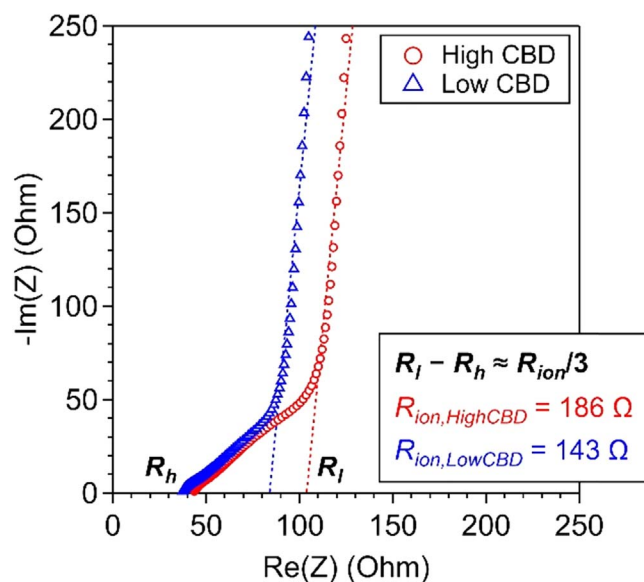
Figure 9. Nyquist plots of graphite/graphite symmetric coin cells containing 10 mM TBAClO$_4$ in EC/DMC (1:1, w/w) electrolyte. High and low CBD loading electrode results are shown with linear fits and calculated R_{ion} values.

have this issue.[56] Nevertheless, the direct measurement on the anode side enables validating the numerical methodology. Cathode values obtained with P2D fit and microstructure analysis were compared in Fig. 8a.

Table IV. Anode microstructure ionic transport coefficients, experimentally measured with EIS, fitted in a macroscale P2D model, and calculated from microstructure analysis.

	EIS		P2D fit		Microstructure analysis	
	High CBD	Low CBD	High CBD	Low CBD	High CBD	Low CBD
ε_{pore}	0.382	0.374	0.33	0.374	0.345	0.375
τ_{pore}^{tp}	4.10 −4.12	2.98 −3.10	4.23	2.674	4.42	2.932
p_{pore}^{tp}	2.466 −2.471	2.108 −2.150	2.3	2.0	2.39	2.097
N_M	10.73–10.79	7.97–8.29	12.81	7.150	12.81	7.82

Initial electrochemical evaluation.—Charge profiles obtained for full-cells (coin-cells) tested at various C-rates are shown in Fig. 10a; dashed lines represent cells using electrodes with high CBD content, while data obtained with low CBD electrodes are shown in solid lines. At slower rates (<C/5), changes in electrode composition have negligible effect in cell behavior. However, as the charging rate increases beyond 1C, higher polarization is observed at high CBD content cell, causing the cells to prematurely meet the charge cutoff and leading to lower capacities. The polarization behavior suggests that the electrode impedance decrease as the CBD content decreases. This expectation is confirmed by the pulse-based impedance measurements in the custom 3-electrode cells (cf. Fig. 10b), which show that the ASI is 20% lower for the cell with the lower CBD

content than the higher CBD cell. Furthermore, the lower cell impedance (cf. Fig. 10c, left) can primarily be attributed to lower cathode impedance (cf. Fig. 10c, middle); only minor changes are observed in the anode impedance (cf. Fig. 10c, right). Data from EIS tests (cf. Fig. 10c) agree with the HPPC test data. As shown in Fig. 10, the cathode plots show high frequency (hf) and mid-frequency (mf) arcs. The hf arc is typically attributed to electrical connectivity of the active material with the conductive carbon particles and the current collector. The smaller arc for the lower CBD electrode suggests better electron conduction, despite the lower carbon content. Overall, the impedance measurements and rate tests at the BOL verify the insights obtained from the microstructure analysis and modeling that improved electrode transport can be
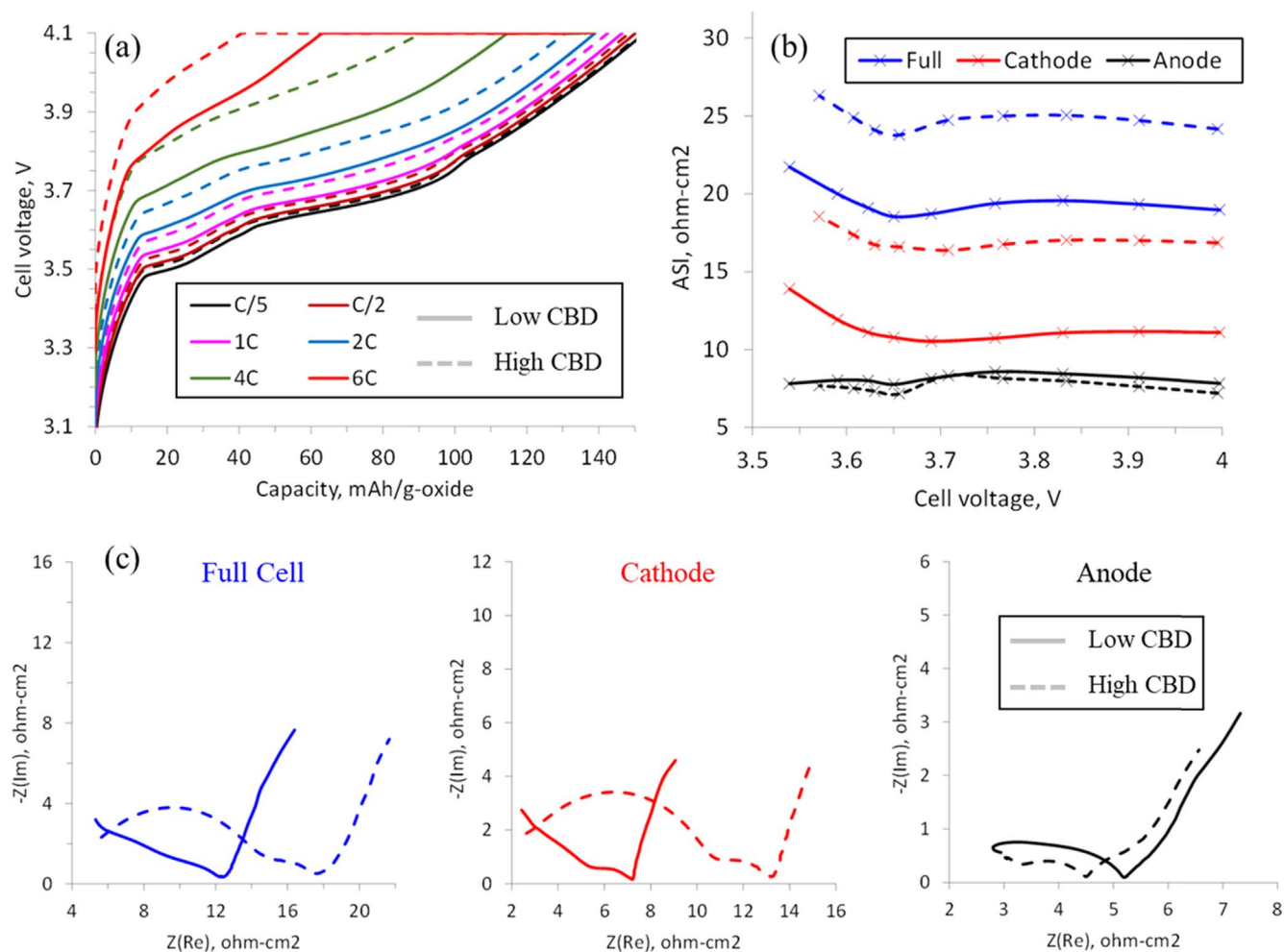
Figure 10. (a) Experimental voltage profiles for coin cells with the lower (solid lines) and higher (dashed lines) CBD contents, charged at various rates (C/5, C/2, 1C, 2C, 4C, 6C). (b) ASI vs cell voltage for the full cell (blue), positive electrode (red) and negative electrode (black): the markers indicate voltage locations of the discharge pulse. (c) EIS plots for the full cell, cathode and anode (custom-made 3-electrode cells); note that the X- and Y-axes scales are different in each plot. In all figures, the solid lines and dashed lines represent cells with the lower and higher CBD contents, respectively.
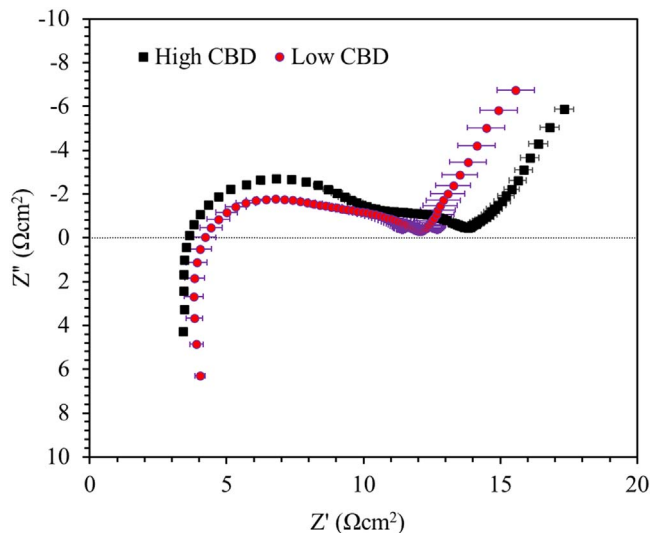
Figure 11. Nyquist plot of low and high CBD SLPC cells at the BOL. The EIS test were performed at 3.9 V. Figure showing average of six cells data with 1σ standard deviation as error bars.

achieved by lowering the CBD content of electrodes. The observed changes are consistent with a decrease in cathode tortuosity in the lower CBD electrode. After these initial tests, electrodes were used in single-layer pouch cells for additional performance tests.

Single layer pouch cells impedance, rate capability and lithium plating.—Evaluation with SLPCs format cells provides additional confirmation of distinct performance improvement. As presented in Fig. 11, the high frequency intercept of the EIS spectrum that captures the ohmic impedance of the cell for the low CBD cells moved slightly towards right than the high CBD spectrum, primarily because of the performance deterioration of the anode (cf. Fig. 10c). However, the mid-frequency depressed semi-circles compressed distinctly for the lower CBD cells, indicating better interfacial processes, primarily in the cathode (cf. Fig. 10c).

The performance improvement observed in Figs. 10 and 11 in the low CBD cell can also be distinctly visible in the fast charge RCTs up to 6C. Figures 12a and 12b present impedance and transport polarizations extracted from post charge voltage relaxations at different C-rates, respectively. Impedance polarization is the immediate relaxation within 12 ms at the end of charge and provides an estimate of cell ohmic and charge transfer polarizations, whereas transport polarization is the difference in voltage between the immediately relaxed state (at 12 ms) and after 15 min rest during post-charge rest[64,65] and captures both liquid and solid-state Li$^+$ transport in the cell. We can observe a distinct decrease in impedance polarization ($\sim$40% decrease) in low CBD cells as compared to high CBD cell. This result when combined with Figs. 10 and 11, can primarily be attributed to improvement in cathode bulk and interfacial processes. The transport polarization in Low CBD cell shows improvements in two different ways: (i) Low CBD cell shows overall lower polarization than high CBD cell, and (ii) unlike high CBD cell that has a distinct transport plateau after 4C, the low CBD cell does not show that plateau up to 6C rate. For this cell design, the plateau after 4C has been linked with Li plating in earlier publications[4,11,66] triggered by sluggish Li + transport through the electrolyte and resulting in distinct non-uniformity in Li + concentration across the electrodes.

Figure 12c through e demonstrate how such heterogeneity in Li + (and material utilization) creates favorable condition for Li plating through modeling. As shown in Fig. 12e, for an aggressive 10 min- 6C CC-CV charging, the SOC reached before the 4.1 V cutoff was only 37% for cells using electrodes with higher CBD content. Cells with lower CBD achieved 55% SOC before the cutoff.

Model predictions are also shown in Fig. 12c as solid lines. The model accurately predicts a significant reduction in overpotential and higher achieved capacity when lowering the CBD content. The model is used to examine the effect of CBD content on lithium plating as shown in Fig. 12d. Plotted is the solid-phase potential minus the liquid phase potential at the graphite/separator interface, which is termed potential for lithium plating. When the potential for lithium plating goes below zero volts, lithium plating is thermodynamically favored. For electrodes with higher CBD, this condition is reached only $\sim$100 s into fast charging and a significant amount of plating is predicted. For the low CBD electrodes, the potential for lithium plating only gets to around +2 mV. A small amount of plating is expected due to heterogeneity effects such as local variations in porosity, tortuosity, particle shape, etc. The improved capacity, reduced overpotential, and reduced lithium plating with lower CBD result from a reduction in electrode tortuosity, and improved cathode bulk and interfacial processes.

Discussion

On microstructure analysis.—Percolation and effective conductivity analysis are purely numerical and rely on a CBD generation algorithm, and thus on an educated guess of the true CBD spatial distribution (though experimental imaging roughly corroborates the generated pattern). An indirect validation is provided with the NMC-CBD specific interface area relative evolution, correlated with the cathode film resistance. However more direct validations are required to conclude on the relevance of CBD generation. One possible approach would be to measure conductivity on lithiated NMC for different loadings to experimentally identify the loading threshold and compare it with the one identified in Fig. 7. Generated CBD patterns (cf Fig. 4) are similar with those generated by Trembacki et al., (cf Figs. 14 and 6 of Refs. 35 and 20, respectively), and to a lesser extent by those generated by Mistry et al.[9,20] Similarity with Trembacki's algorithm was expected since both methods aim to build bridge between neighboring particles, while differences with Mistry's algorithm arise due to the intrinsic stochasticity of the authors' method and its apparent indiscrimination approach between small and large pores. Interestingly, CBD spatial distribution obtained from the manufacturing modeling approach seems also to let the largest pores free of CBD (cf Fig. 6 of Ref. 42). Although, a definitive statement would require comparing same geometries. Eventually, it is expected the best representation would be achieved through manufacturing modeling to take into consideration the specificities of each process path (e.g., solvent free[67]). Although significant efforts are still required to model accurately each step (as mentioned earlier, the drying step is not well understood[44]), and validation through imaging is still challenging whatever the CBD generation methods.

Percolation and conductivity analyses were all performed with the NMC spatial distribution of the baseline CBD loading, implicitly assuming that the NMC spatial distribution is independent from CBD loading, which may not be accurate, especially for the very low loading. Therefore, the percolation and effective conductivity prediction's validity is decreasing (with an unknown error) from the high (i.e., baseline) to the low CBD loading. CBD weight recommendation is based on the pristine electrode, without aging consideration (e.g., delamination). Therefore, the values provided with this analysis should be considered as a lower bound of the optimal CBD loading.

CBD uniform and heterogeneous distribution representations are equivalent to predict the effective transport properties for different CBD loadings, if fitted adequately. This indicates that once fitted for the same point, both approaches keep their coherence suggesting a robust fitting. For averaged transport properties, the higher complexity of the CBD heterogeneous distribution is thus not required, and a simple uniform representation is enough to model averaged performance. However, for sub-millimeter local electrochemical response, the two approaches are not equivalent, as spatial

distribution of the high conductivity CBD controls the solid potential field, albeit it is out of the scope of this article. As well, a uniform representation is, by definition, unable to predict local onset of degradation mechanisms. The lower-scale coefficient fitting of CBD uniform and heterogeneous approaches, while equivalent for the effective transport coefficients, should not be interpreted equally. Indeed, the very high nanoporosity fitted for the uniform approach does not match with image-based measurement, suggesting that the uniform approach is an oversimplification that results in overfitted lower scale coefficients. On the other hand, the heterogeneous approach is based on the above mentioned measured nanoporosity and on the semi-validated CBD spatial distribution, resulting in more plausible lower-scale coefficients. Furthermore, the calculated CBD transport properties are in agreement with Zielke et al.,[31] from FIB-SEM imaging, suggesting the heterogenous distribution is accurate.

The microstructure scale analysis provided an underestimation of the fitted Bruggeman exponent reduction (∼60%, cf Fig. 8a). Such discrepancy could be attributed to the assumption that $p^{nano,u}$, $p^{nano,h}$ are constant for the different CBD loading investigated, especially considering the very large CBD loading relative variation. Alternatively, the underestimation could be attributed to a change of the CBD spatial distribution pattern from high to low loading, for instance from agglomerates to fiber-like distribution, respectively, the latter being less penalizing for ionic diffusion. Such possible loading-dependent shift in the CBD pattern distribution would require algorithms specific for each loading, while in our work the same generation algorithm was used to investigate both the low and high CBD loading. Other factors (e.g., impact of CBD on the specific surface area) can also contribute to this result. Lastly, the fitted Bruggeman exponent used in the P2D model has some uncertainty, due to the model sensitivity with this parameter, and should be then considered as an estimate, as further discussed by K. S. Mayilvahanan et al.[28]

On cell performance.—An optimal amount of CBD has been shown to significantly improve the initial fast charge performance of graphite-NMC cells. A combination of P2D modeling and direct tortuosity measurements show optimizing CBD loading results in higher fast charge acceptance due to a reduction in electrode tortuosity. Further, the lower CBD content results in less blocking/coverage of the active material surface resulting in lower interfacial resistances as measured by EIS and HPPC. P2D modeling combined
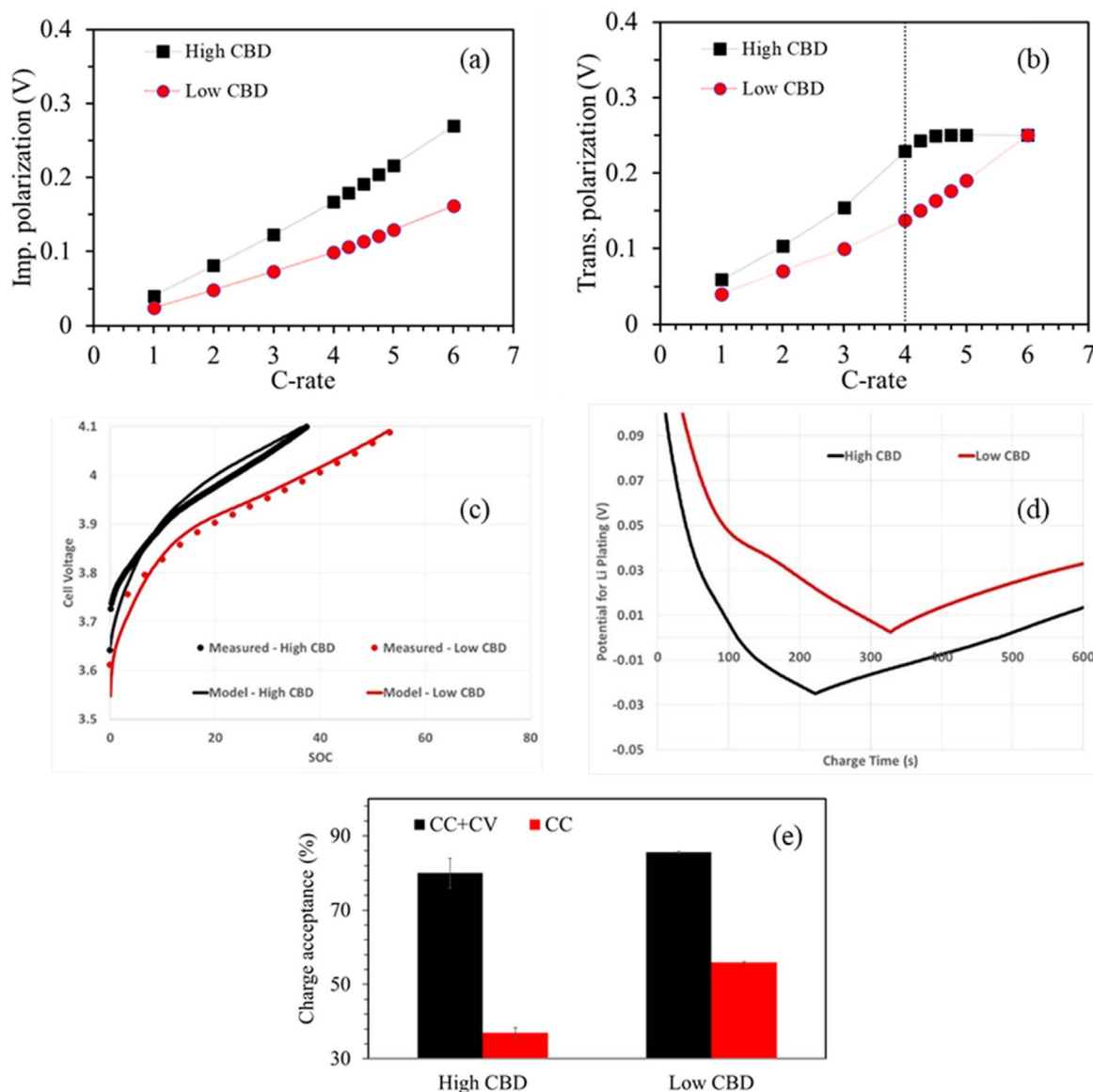
Figure 12. BOL electrochemical performance for pouch cells with different CBD loading: (a) cell impedance polarization, (b) cell transport polarization, (c) cell voltage and (d) potential for plating for a 6C-CC charge profile (4.1 V, 10 min cutoff), (e) 1st cycle charge CC-CV charge acceptance in 10 min (here capacities were scaled by BOL C/1 capacity).

with experimental SLPC's data concludes that the optimized CBD content significantly reduces the amount of lithium plating at beginning of life. This prediction needs to be verified with post-mortem analysis after long-term fast charge cycling. Besides improving fast charge acceptance, the reduction in CBD content improves the volumetric energy density and to a lesser extent specific energy density of cells.

One consideration not discussed above, is the effect of CBD content on the mechanical resiliency of electrodes. If the CBD content is too low, electrodes can suffer from more particle isolation and delamination. Peel tests[68] could be performed to quantify the cohesion strength of each electrode for various CBD loadings and identify a threshold, if any.

Early cycling experiments indicated performance degradation for the low CBD loading cell despite initial better performances. Post-mortem analysis revealed anode delamination from the current collector, while cathode side was undamaged. The current recommendation is therefore to keep the high CBD loading for the anode, while reducing it to the proposed level determined in this work for the cathode. Excellent long-term fast-charge cycling with these loadings have been achieved by using low CBD cathodes combined with alternative methods to reduce ionic resistance in anode (bi-layer, laser ablation, etc). Long-term fast charge cycling is not currently included as it will be the subject of a future paper.

Conclusions

Impact of carbon-black binder (CBD) loading on electrochemical performance has been investigated through a wide array of numerical methods and experiments. These range from the representation, characterization, and homogenization of electrode microstructures, battery macroscale modeling, and impedance and rate capabilities measurements on various cell formats. The combined work provides information on connectivity/percolation of the solid network, effective solid conductivity and ionic diffusivity, interfacial area, cell capacity, lithium plating, impedance, and transport polarization at the beginning of life (BOL). The collected results depict a detailed, multifaceted, overview of the CBD loading impact on the cell behavior, with significant performance improvements reported for the low CBD loading compared with the high CBD baseline investigated in this work. Main findings are summarized in the next paragraphs.

Percolation.—To remedy for the lack of representative imaging that includes the CBD, an in-house open-source generation algorithm has been developed to add the additive phase on top of an existing active material spatial distribution obtained with X-ray CT. The subsequent connectivity analysis revealed that nearly all cathode particles are connected to the current collector for the investigated loadings. However, a moderate CBD volume fraction threshold, estimated between 3.9% and 5.8%, is required to ensure active materials are connected to the current collector through an interrupted line of CBD material. This prevents the electrode to be limited by the poor conductivity of the NMC particles. The NMC baseline CBD volume fraction, 13.8% (10 wt% CBD), has been then found unnecessarily high, based on percolation ground, and a reduced CBD loading, 5.2% (4 wt%) has been recommended.

Effective transport.—Effective solid conductivity has been calculated for different CBD loading, considering the NMC bulk conductivity variation with its SOC. Model predicts high CBD electrode effective conductivity along the thickness, $K_s^{eff, tp}$, to be quite insensitive with NMC SOC, with values contained in the same order of magnitude: $K_s^{eff, tp} = 1e^{-2}$ $S.cm^{-1}$ and $0.5e^{-2}$ $S.cm^{-1}$, respectively at low (0.25) and high (0.9–1.0) intercalation fraction. Conversely, low CBD electrode effective conductivity is predicted to vary by 1 or 2 order of magnitude with the NMC intercalation fraction: $K_s^{eff, tp} = 3.5e^{-3}$ $S.cm^{-1}$, $3.5e^{-4} - 5.5e^{-4}$ $S.cm^{-1}$, and

$0.3e^{-4} - 1.6e^{-4}$ $S.cm^{-1}$ respectively at low (0.25), high (0.9 considering potential Li loss at the anode side) and unit (1.0) intercalation fraction For loading below the proposed low CBD loading, conductivity shrinks towards NMC-level conductivity or below as loading is insufficient to reach the desired connectivity and effective conductivity is limited by the NMC particles.

CBD loading reduction led to an improvement of the ionic transport in the cathode, even though porosity has been reduced (active material loading was increased), with a Bruggeman exponent p_{pore}^{tp} reduction from 2.0 to 1.8 (P2D fitting), of which 60% is explained by the microstructure analysis. Significant Bruggeman exponent reduction has been fitted as well for the graphite, from 2.3 to 2.0 (from 8 wt% to 4 wt%), in good agreement with the values calculated from microstructure homogenization. Symmetric cell measurements show improved ionic transport property for the anode, from high CBD to low CBD (p_{pore}^{tp} from ~2.5 to ~2.1) even though porosity decreased slightly. Improving the effective ionic transport by reducing the porosity through a reduction of the CBD loading and an increase of the active material loading demonstrates that the CBD impacts significantly more negatively the effective ionic transport than the active material, and that a tradeoff between the two loadings is highly beneficial for the ionic transport. The result also challenges the assumption that tortuosity is always a decreasing function with porosity for a given electrode material.

Carbon-binder representation.—CBD uniform and heterogeneous distribution are equivalent for macroscale ionic transport coefficient p_{pore}^{tp}, at the condition their respective nanoscale coefficients have been fitted prior for a given CBD loading, through reverse homogenization as done in this work. Nevertheless, the uniform distribution requires unrealistic high nanoporosity that contradicts observation, indicating such approach is an oversimplification that results in overfitting of the nanoscale coefficients. CBD heterogenous distribution, associated with a CBD nanoporosity of 47%, and fitted with macroscale coefficients (P2D), predicts the normalized effective diffusion coefficient of the CBD at the microstructure scale X_{CBD}^{μ}/X_e^{bulk} to be equal to 0.280 and 0.139, which correspond to CBD tortuosity $\tau^{nano,h}$ of 1.67 and 3.37, and Bruggeman exponent $p^{nano,h}$ of 1.68 and 2.61, respectively for NMC and graphite.

Impedance measurements.—Area-specific impedance (ASI) was measured 20% lower for the low CBD cell in the custom-3-electrode setup, with lower cell impedance attributed to the lower cathode impedance. Data from electrochemical impedance spectroscopy (EIS) tests agree with the HPPC test data. Furthermore the 20% ASI reduction is coherent with the 25% NMC-CBD interface area reduction calculated from the microstructure analysis from high to low CBD cathode. Single layer pouch cell (SLPC) Nyquist plot reveals improvement in ohmic impedance due to better electronic and ionic conductance of the solid and liquid phases of lower CBD cells, and better interfacial processes mainly in the cathode, which corroborates the custom-3-electrode measurement. SLPC impedance polarization exhibits a significant reduction from high to low CBD cells (−40%), attributed to improvement in cathode bulk and interfacial processes. As well, SLPC transport polarization is lower for low CBD cells, without plateau at 6C (unlike for high CBD cells) which suggests no lithium plating.

Rate capability and lithium plating.—Coin cell screening shows higher polarization measured for the high CBD content cell for charging rate above 1C, causing the cells to prematurely meet the charge cutoff and leading to lower capacities: 40 and 63 mAh g^{-1}-oxide at the end of the 6C constant current, respectively for high and low CBD. SLPC 6C CC-CV charging also demonstrate capacity improvement, from 37% (80%) to 55% (86%), respectively for high and low CBD cells at the cutoff voltage (at the end of the

10 min CC-CV), with measured cell voltage in good agreement with model. Model also predicts lithium plating thermodynamically favorable condition to be avoided with the low CBD cell, as the potential for plating never goes below +2 mV, while it reaches the threshold after 100 s for the high CBD loading. Performance improvements are attributed to the reduced electrode tortuosity, cathode film resistance, and cathode thickness.

ORCID

Francois L. E. Usseglio-Viretta https://orcid.org/0000-0002-7559-8874
Andrew M. Colclasure https://orcid.org/0000-0002-9574-5106
Alison R. Dunlop https://orcid.org/0000-0001-9785-0375
Stephen E. Trask https://orcid.org/0000-0002-0879-4779
Andrew N. Jansen https://orcid.org/0000-0003-3244-7790
Daniel P. Abraham https://orcid.org/0000-0003-0402-9620
Marco-Tulio F. Rodrigues https://orcid.org/0000-0003-0833-6556
Eric J. Dufek https://orcid.org/0000-0003-4802-1997
Tanvir R. Tanim https://orcid.org/0000-0002-1864-6868
Yeyoung Ha https://orcid.org/0000-0003-2679-2539
Kandler Smith https://orcid.org/0000-0001-7011-0377

References

1. C. Michelbacher et al., *J. Power Sources*, **367**, 214 (2017).
2. A. M. Colclasure, A. R. Dunlop, S. E. Trask, B. J. Polzin, A. N. Jansen, and K. Smith, *J. Electrochem. Soc.*, **166**, A1412 (2019).
3. D. C. Robertson, L. Flores, A. R. Dunlop, S. E. Trask, F. L. E. Usseglio-Viretta, A. M. Colclasure, Z. Yang, and I. Bloom, *Energy Technol-ger*, **9**, 2000666 (2021).
4. A. M. Colclasure et al., *Electrochim. Acta*, **337**, 135854 (2020).
5. F. L. Usseglio-Viretta et al., *J. Electrochem. Soc.*, **165**, A3403 (2018).
6. M. Doyle, *J. Electrochem. Soc.*, **140**, 1526 (1993).
7. M. Doyle and J. Newman, *Electrochim. Acta*, **40**, 2191 (1995).
8. J. Newman and W. Tiedemann, *Aiche J*, **21**, 25 (1975).
9. A. N. Mistry, K. Smith, and P. P. Mukherjee, *Acs Appl Mater Inter*, **10**, 6317 (2018).
10. F. L. E. Usseglio-Viretta, D. Finegan, A. M. Colclasure, T. Heenan, D. P. Abraham, P. R. Shearing, and K. Smith, *J. Electrochem. Soc.*, **167**, 100513 (2020).
11. P. R. Chinnam et al., *ACS Appl. Energy Mater.*, **4**, 9133 (2021).
12. T. R. Tanim et al., *Adv. Energy Mater.*, 2103712 (2022).
13. N. Epstein, *Chem. Eng. Sci.*, **44**, 777 (1989).
14. B. Tjaden, S. J. Cooper, D. J. Brett, D. Kramer, and P. R. Shearing, *Current Opinion in Chemical Engineering*, **12**, 44 (2016).
15. S. Ahmed et al., *J. Power Sources*, **367**, 250 (2017).
16. B. Tjaden, D. J. Brett, and P. R. Shearing, *Int. Mater. Rev.*, **63**, 47 (2016).
17. B. Ghanbarian, A. G. Hunt, R. P. Ewing, and M. Sahimi, *Soil Sci. Soc. Am. J.*, **77**, 1461 (2013).
18. L. Shen and Z. Chen, *Chem. Eng. Sci.*, **62**, 3748 (2007).
19. F. L. E. Usseglio-Viretta, W. Mai, A. M. Colclasure, M. Doeff, E. Yi, and K. Smith, *Electrochim. Acta*, **342**, 136034 (2020).
20. B. L. Trembacki, A. N. Mistry, D. R. Noble, M. E. Ferraro, P. P. Mukherjee, and S. A. Roberts, *J. Electrochem. Soc.*, **165**, E725 (2018).
21. C. Bae, C. K. Erdonmez, J. W. Halloran, and Y. Chiang, *Adv. Mater.*, **25**, 1254 (2013).
22. J. B. Habedank, L. Kraft, A. Rheinfeld, C. Krezdorn, A. Jossen, and M. F. Zaeh, *J. Electrochem. Soc.*, **165**, A1563 (2018).
23. L. Hille, L. Xu, J. Keilhofer, S. Stock, J. Kriegler, and M. F. Zaeh, *Electrochim. Acta*, **392**, 139002 (2021).
24. M. R. Amin, B. Delattre, A. P. Tomsia, and Y.-M. Chiang, *ACS Appl. Energy Mater.*, **1**, 4976 (2018).
25. W. Mai, F. L. E. Usseglio-Viretta, A. M. Colclasure, and K. Smith, *Electrochim. Acta*, **341**, 136013 (2020).
26. F. Usseglio-Viretta and K. Smith, *ECS Trans.*, **77**, 1095 (2017).
27. J. Billaud, F. Bouville, T. Magrini, C. Villevieille, and A. R. Studart, *Nat. Energy*, **1**, 16097 (2016).
28. K. S. Mayilvahanan et al., *J. Electrochem. Soc.*, **168**, 070537 (2021).
29. L. S. de Vasconcelos, R. Xu, J. Li, and K. Zhao, *Extreme Mech Lett*, **9**, 495 (2016).
30. S. R. Daemi, C. Tan, T. Volkenandt, S. J. Cooper, A. Palacios-Padros, J. Cookson, D. J. L. Brett, and P. R. Shearing, *ACS Appl. Energy Mater.*, **1**, 3702 (2018).
31. L. Zielke, T. Hutzenlaub, D. R. Wheeler, C. Chao, I. Manke, A. Hilger, N. Paust, R. Zengerle, and S. Thiele, *Adv. Energy Mater.*, **5**, 1401612 (2015).
32. S. Vierrath, L. Zielke, R. Moroni, A. Mondon, D. R. Wheeler, R. Zengerle, and S. Thiele, *Electrochem. Commun.*, **60**, 176 (2015).
33. M. Kroll, S. L. Karstens, M. Cronau, A. Höltzel, S. Schlabach, N. Nobel, C. Redenbach, B. Roling, and U. Tallarek, *Batter Supercaps*, **4**, 1363 (2021).
34. S. Jaiser, J. Kumberg, J. Klaver, J. L. Urai, W. Schabel, J. Schmatz, and P. Scharfer, *J. Power Sources*, **345**, 97 (2017).
35. B. L. Trembacki, D. R. Noble, V. E. Brunini, M. E. Ferraro, and S. A. Roberts, *J. Electrochem. Soc.*, **164**, E3613 (2017).
36. S. Jaiser, M. Müller, M. Baunach, W. Bauer, P. Scharfer, and W. Schabel, *J. Power Sources*, **318**, 210 (2016).
37. Z. Jiang et al., *Nat. Commun.*, **11**, 2310 (2020).
38. J. Laurencin, R. Quey, G. Delette, H. Suhonen, P. Cloetens, and P. Bleuet, *J. Power Sources*, **198**, 182 (2012).
39. S. J. Cooper, A. Bertei, P. R. Shearing, J. A. Kilner, and N. P. Brandon, *Softwarex*, **5**, 203 (2016).
40. T. Kanit, S. Forest, I. Galliet, V. Mounoury, and D. Jeulin, *Int. J. Solids Struct.*, **40**, 3647 (2003).
41. M. Chouchane, A. Rucci, T. Lombardo, A. C. Ngandjong, and A. A. Franco, *J. Power Sources*, **444**, 227285 (2019).
42. A. C. Ngandjong, T. Lombardo, E. N. Primo, M. Chouchane, A. Shodiev, O. Arcelus, and A. A. Franco, *J. Power Sources*, **485**, 229320 (2021).
43. M. Nikpour, B. A. Mazzeo, and D. R. Wheeler, *J. Electrochem. Soc.*, **168**, 120518 (2021).
44. M. Nikpour, N. Barrett, Z. Hillman, A. I. Thompson, B. A. Mazzeo, and D. R. Wheeler, *J. Electrochem. Soc.*, **168**, 060547 (2021).
45. I. Srivastava, D. S. Bolintineanu, J. B. Lechman, and S. A. Roberts, *Acs Appl Mater Inter*, **12**, 34919 (2020).
46. G.-H. Kim, K. Smith, J. Lawrence-Simon, and C. Yang, *J. Electrochem. Soc.*, **164**, A1076 (2017).
47. D. E. Stephenson, B. C. Walker, C. B. Skelton, E. P. Gorzkowski, D. J. Rowenhorst, and D. R. Wheeler, *J. Electrochem. Soc.*, **158**, A781 (2011).
48. F. L. E. Usseglio-Viretta, P. Patel, E. Bernhardt, A. Mistry, P. P. Mukherjee, J. Allen, S. J. Cooper, J. Laurencin, and K. Smith, *Softwarex*, **17**, 100915 (2022).
49. F. Usseglio-Viretta, P. Patel, E. Bernhardt, J. Allen, A. Mistry, P. P. Mukherjee, S. J. Cooper, J. Laurencin, and K. Smith, MATBOX: an open-source microstructure analysis toolbox for microstructure generation, segmentation, characterization, visualization, correlation, and meshing https://github.com/NREL/MATBOX_Microstructure_analysis_toolbox.
50. J. Joos, M. Ender, I. Rotscholl, N. H. Menzler, and E. Ivers-Tiffée, *J. Power Sources*, **246**, 819 (2014).
51. J. Wang, J. K. Carson, M. F. North, and D. J. Cleland, *Int. J. Heat Mass Transfer*, **49**, 3075 (2006).
52. R. Amin and Y.-M. Chiang, *J. Electrochem. Soc.*, **163**, A1512 (2016).
53. F. Usseglio-Viretta, J. Laurencin, G. Delette, J. Villanova, P. Cloetens, and D. Leguillon, *J. Power Sources*, **256**, 394 (2014).
54. L. D. Gelb and K. Gubbins, *Langmuir*, **15**, 305 (1999).
55. E. J. McShane, A. M. Colclasure, D. E. Brown, Z. M. Konz, K. Smith, and B. D. McCloskey, *ACS Energy Lett.*, **5**, 2045 (2020).
56. J. Landesfeind, J. Hattendorff, A. Ehrl, W. A. Wall, and H. A. Gasteiger, *J. Electrochem. Soc.*, **163**, A1373 (2016).
57. Z. Yang et al., *J. Power Sources*, **521**, 230961 (2022).
58. D. W. Dees, A. N. Jansen, and D. P. Abraham, *J. Power Sources*, **174**, 1001 (2007).
59. M.-T. F. Rodrigues, K. Kalaga, S. E. Trask, D. W. Dees, I. A. Shkrob, and D. P. Abraham, *J. Electrochem. Soc.*, **166**, A996 (2019).
60. P. P. Paul et al., *Energ Environ Sci*, **14**, 4979 (2021).
61. S. E. Trask, Y. Li, J. J. Kubal, M. Bettge, B. J. Polzin, Y. Zhu, A. N. Jansen, and D. P. Abraham, *J. Power Sources*, **259**, 233 (2014).
62. D. A. Rajon, P. W. Patton, A. P. Shah, C. J. Watchman, and W. E. Bolch, *Med. Phys.*, **29**, 682 (2002).
63. F. Pouraghajan, H. Knight, M. Wray, B. Mazzeo, R. Subbaraman, J. Christensen, and D. Wheeler, *J. Electrochem. Soc.*, **165**, A2644 (2018).
64. T. R. Tanim et al., *J. Electrochem. Soc.*, **166**, A1926 (2019).
65. X. Yang and T. Miller, *SAE Technical Paper*, 2017-01-1204 (2017).
66. B.-R. Chen, M. R. Kunz, T. R. Tanim, and E. J. Dufek, *Cell Reports Phys Sci*, **2**, 100352 (2021).
67. B. Ludwig, J. Liu, Y. liu, Z. Zheng, Y. Wang, and H. Pan, *J Micro Nano-manufacturing*, **5**, 040902 (2017).
68. A. M. Gaikwad and A. C. Arias, *Acs Appl Mater Inter*, **9**, 6390 (2017).